UNIVERSITÀ DEGLI STUDI DI PADOVA

DIPARTIMENTO DI SCIENZE CHIMICHE

CORSO DI LAUREA MAGISTRALE IN SCIENZA DEI MATERIALI

TESI DI LAUREA MAGISTRALE

Micropatterning of a PSF electrospun anti-biofouling membrane for water filtration via Hot Embossing

Relatore: Edmondo Maria Benetti

Co-relatore: Susan Kelleher

Laureando: Daniele Masi

Anno Accademico 2022-2023

Table of Contents

Acknowledgements

Dopo un percorso durato anni, si chiude per me un capitolo importante. Riassumere in una manciata di righe tutto quello che devo a chi mi ha aiutato e sostenuto durante questo periodo sarebbe semplicemente riduttivo. Anni fa entrai per la prima volta in un'aula del Dipartimento di Scienze Chimiche, in via Marzolo, e pochi giorni fa ho chiuso per l'ultima volta la porta del laboratorio X249 della Dublin City University. Le persone con cui ho condiviso tutto quello che c'è stato in mezzo a questi due eventi fanno parte di questo lavoro, e probabilmente lo sanno.

Alla mia famiglia, ai miei amici più cari, al Kelleher Group. Grazie a tutti.

Abstract

One of the most ambitious goals of the last decades is increasing drinkable water availability in poor countries. Among a number of strategies for water treatment, pressure-driven filtration using polymeric membranes is a promising approach as it is green, scalable, and cheap. However, there are some major limitations. Membrane fouling is a critical issue in water filtration as it limits the efficiency and durability of membranes; strategies against the effect of several types of fouling have been studied by many research groups so far. Biofouling is the unwanted formation and growth of a biofilm, and the prevention of this phenomenon needs to be tackled to get performant membranes; among various ways of inhibiting biofouling, bioinspired micro- and nanopatterns have been found to be really effective, so structuring the surfaces of membranes could be a non-selective method for discouraging bacteria proliferation to achieve better performances and increase their durability. Membranes, as well as anti-biofouling and antibacterial surfaces, need to be tested. In the present work, the developing of a method for Water Contact Angle measuring without a goniometer, and a standard procedure for curing Poly Ethylene Glycol Diacrylate and Poly Propylene Glycol Diacrylate for antibacterial tests, were found. The developing of a procedure for molding polymers for analysis of an antibacterial bioinspired nanopattern has been initiated; the optimization of Hot Embossing (HE) processes for engraving a micro- and a nanopattern on microporous Polysulfone (PSF) mats obtained by electrospinning was carried out.

Abstract in Italiano

Uno degli obbiettivi più ambiziosi degli ultimi decenni è aumentare la disponibilità di acqua potabile nei paesi più poveri. Fra diverse strategie adottate per il trattamento dell'acqua, la filtrazione tramite membrane polimeriche che utilizza la differenza di pressione come driving force è un approccio promettente in quanto economico, sostenibile e scalabile. Tuttavia, ci sono alcune rilevanti limitazioni. Il fouling (incrostazione) è un problema nei processi di filtrazione dell' acqua, in quanto limita l'efficienza e la durabilità delle membrane. Ad oggi, sono stati studiati approcci per diversi tipi di fouling da molti gruppi di ricerca. Il biofouling consiste nella formazione e crescita indesiderate di biofilm, e la prevenzione di questo fenomeno è fondamentale per ottenere membrane performanti; fra vari metodi per inibire il biofouling, si è trovato che l'impiego di micro- e nanopattern bioispirati sia molto efficace; micro- o nanostrutturare la superficie di una membrana potrebbe essere un metodo non selettivo per scoraggiare la proliferazione di batteri, e ottenere dunque performance migliori e maggiore durabilità della membrana stessa. Sia le superfici strutturate che le membrane devono essere sottoposte a vari test. In questo lavoro, sono stati sviluppati un metodo per misurare il Water Contact Angle (WCA) senza l'uso di un goniometro per WCA, e una procedura standard per effettuare cross-linking tramite irraggiamento UV di Polietilen Glicole Diacrilato e Polipropilen Glicole Diacrilato. È stata studiata una procedura per il nanostrutturare la superficie degli stessi polimeri al fine di studiare gli effetti antibatterici del nanopattern bioispirato; sono stati condotti esperimenti per strutturare un processo di Hot embossing: lo studio si è focalizzato sui parametri utili a conferire un micropattern e il nanopattern bioispirato a un *mat* polimerico microporoso in polisolfone PSF ottenuto mediante elettrospinning.

List of abbreviations

AFM - Atomic Force Microscopy

AR - Aspect Ratio

CA - Contact Angle

CNI - Compact Nanoimprint

FT - Fourier Transform

HE - Hot embossing

MF - Microfiltration

NF - Nanofiltration

PDMS - Polydimethylsiloxane

PEG - Poly Ethylene Glycol

PEGDA - Poly Ethylene Glycol Diacrylate

PFOCTS - Trichloro(1H,1H,2H,2H-perfluoro-octyl)silane

PLA - Polylactic Acid

PPG - Poly Propylene Glycol

PPGDA - Poly Propylene Glycol Diacrylate

PSF - Polysulfone

RO - Reverse Osmosis

SEM - Scanning Electron Microscopy

UF - Ultrafiltration

WCA - Water Contact Angle

WF - Water Filtration

1. Introduction

Water is an essential resource for human activities and life on Earth. Population growth and water contamination call for new strategies for clean drinking water supply: about 1.1 billion people currently lack access to drinkable water and 2.7 billion people for at least one month per year; in developing countries where environmental issues are caused by recent industrialization, millions of people are suffering from diseases caused by contaminated water supplies[1].

Global water resources are classified into Unconventional Water Resources (UCWRs) and Conventional Water Resources (CWRs). UCWRs such as wastewater and seawater can be cleaned from contaminants; CWRs are directly providing fresh water from natural sources such as groundwater, rivers, and lakes. CWRs are frequently converted into UCWRs by food industries, textile manufacturing, refineries, automotive industries, and others. In addition, industrial activities often lead to mixing UCWRs with CWRs, bringing an overall decrease of uncontaminated water, which does not meet the requirements of the global demand[2].

In recent years, research on improving membrane technology has increased for these reasons; several water treatment methods have been studied in the past decades for purifying water from different pollutants and desalinization. However, most of them are chemistry-based and often require complex equipment, expensive operations, and high energy consumption. Filtration with membranes is a promising approach for the sustainable purification of UCWRs as it does not involve reactions, it is simple in its basic operations, cheap, easily scalable, highly selective, and requires nearly chemical-free treatments[2–4].

1.1.Membranes for Water Filtration

Membranes for water filtration (WF) are structures either polymeric (organic) based, inorganic (ceramic) based, or hybrids. They are semipermeable or selective barriers for pollutants or metals to be recovered: while the fluid to be purified is transferred from the inlet to the outlet of a membrane, the passage of a target group of species that need to be removed is hindered.

The portion of fluid which is passing through is called permeate, whilst the retained species are called retentate[3].

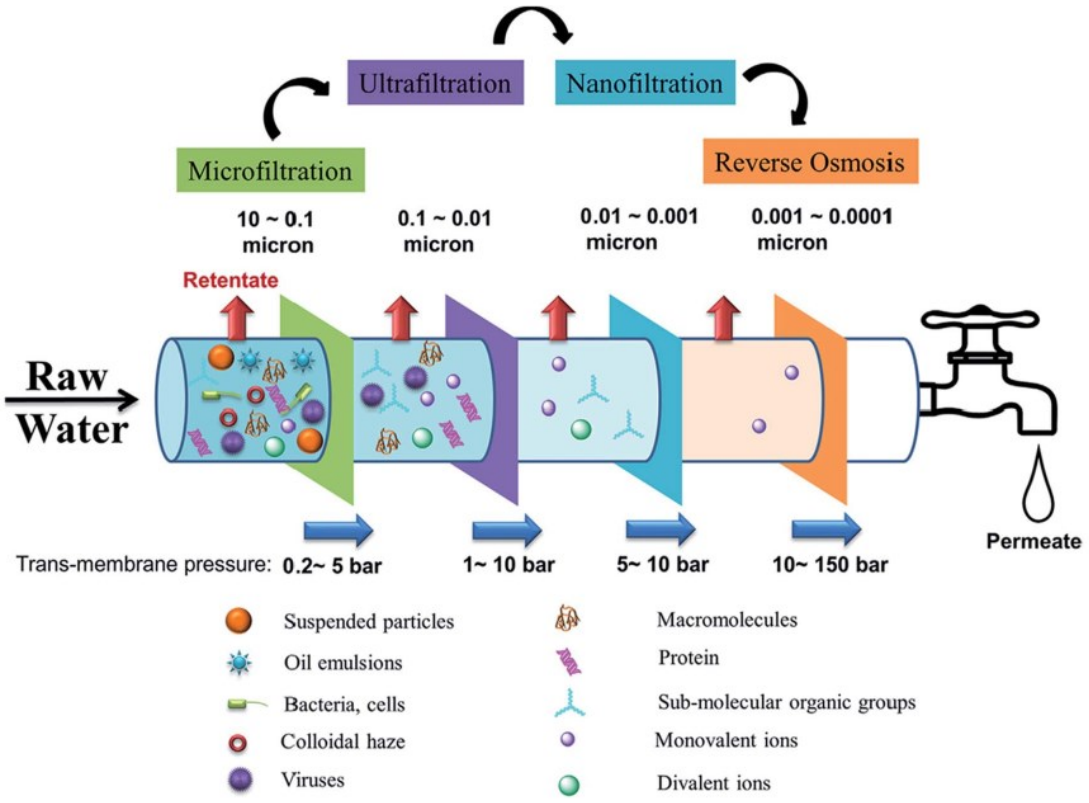

Figure 1: scheme of the steps of water filtration; types of pollutants to be filtered, and classification of membranes for water filtration according to the size of the retentate

The driving forces for fluid flow can be temperature, chemical potential, or pressure; the focus of this paragraph will be on pressure-driven filtration. Membranes for pressure-driven filtration can be classified depending on their rejection capability of pollutants, therefore on their application: details about Microfiltration MF, Ultrafiltration (UF), Nanofiltration (NF), and Reverse Osmosis (RO) membranes pollutants to be filtered out and their size are summarized in Fig.1. Contaminants like bacteria, yeasts, and large colloidal particles are filtered from 0.1 to 10 μm pores membrane (Microfiltration); some viruses, smaller dispersed particles, and macromolecules like proteins, starches or suspended solids are filtered by about 0.05 to 0.1 μm pores (Ultrafiltration); Nanofiltration and Reverse Osmosis membranes are non-porous or

pores-poor filters in which species dissolve and diffuse; viruses, organic solutes, dissolved salts can be filtered out with these methods. As a general rule, the smaller the species to be filtered, the higher the pressure to be applied: a 02-5 bar pressure is applied for MF, 1-10 bar for UF, 5-10 bar for NF, and 10-150 bar for RO.

As mentioned before, many advantages of using membranes make them an attractive option for water purification, but there are some intrinsic drawbacks with this technology: the most problematic one is fouling, unwanted sediments that rapidly worsen the performance of membranes[5–7].

1.2.Fouling

Fouling of membranes is the unwanted deposition of substances on the surface of the membrane during the separation process, which leads to a rapid decrease of the permeate flux and high reduction in filtration efficiency; fouling is the main reason for which membranes need to be cleaned or substituted frequently[8,9].

Membrane foulants can be categorized into three types based on: their components (inorganic, organic or bio-foulants), the ease to remove them (reversible, irreversible or irremovable), and the fouling mechanism (non-migratory, spreadable and proliferative foulants). The general mechanism of fouling can be summarized into three steps[8]: approach of the foulants in the inlet flux to the membrane surface by diffusion and transmembrane forces (1), adsorption/deposition on the membrane's surface or into the pores (2), and aggregation, spreading or film/gel growth depending on the nature of the foulants (3)[10].

The debate in the following will be focused on biofouling, as tackling this issue is the field of research of this group.

1.3.Biofouling

Biofouling consists of microorganisms deposition and the resulting biofilm growth (Fig.2). Three steps can be identified in biofouling mechanism: adhesion, maturation, and dispersion.

The first step can be sub-divided into two stages; firstly, single bacterial cells loosely interact with the surface via physicochemical forces; this step is called reversible attachment. Then, the cells start expressing extracellular polymeric substances (EPS), which is mainly composed of polysaccharides and proteins, that facilitates the adhesion with the surface leading to an irreversible attachment within a few minutes. At this stage, the biofilm is "mature"; the biofilm matrix is composed of cells, EPS, and nutrients that are able to circulate within channels inside the matrix; in this way, interspecies bacteria can share metabolic substrates and survive in the matrix. Finally, some aggregates and bacteria are released from the matrix and then they reach a different region of the surface; this process make the spreading and growing of a stable biofilm more rapid[9,11,12].

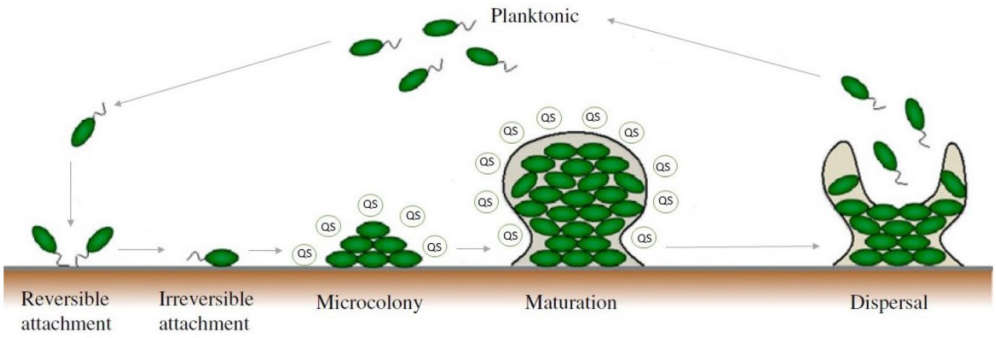

Figure 2: scheme of biofilm formation

Cells also produce molecules that help this mechanism proceed, bacterial quorum sensing (QS): they are responsible for cell-to-cell communication in the biofilm and regulate its growth.

Biofilm formation dramatically affects the performance of membranes, because it grows in the pores, so it reduces the permeate flux and might deteriorate the membranes; as a consequence, membranes must be replaced or cleaned very often. That is why scientists are developing strategies for biofouling inhibition[9].

1.4.Bioinspired anti-biofouling micro- and nanopatterned surfaces

Various strategies for eliminating or inhibiting membrane fouling have been studied so far; they are generally distinguished as passive and active. Passive anti-fouling strategies aim to prevent pollutants from adhering to the surfaces, without affecting foulants directly. Active anti-fouling strategies target the intrinsic properties of foulants; they inactivate cells activity and degrade the chemical structure of the foulants to make them harmless[2,11].

Most of the current anti-biofouling applications rely on releasing biocidal compounds (active), surfaces with chemical-enhanced hydrophilicity or hydrophobicity, and morphological structure modifications (passive). There are some drawbacks and limitations in most of these approaches: harmful or non-green species can be released when chemical treatment is involved in biofilm degradation; chemical-treated anti-biofouling membranes can deteriorate when used with seawater or other types of wastewaters with substantial efficiency loss; structured morphologies are usually less efficient than other approaches[11,13]. A novel general approach to this problem is becoming established: the employing of bioinspired structures showing anti-biofouling activity is a promising strategy that caught the attention of researchers in this field in the last decade (Graph 1).

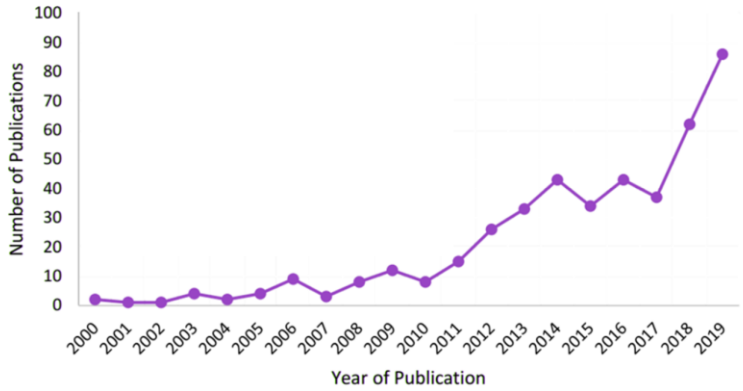

Graph 1: publications per year on bioinspired anti-biofouling structure-based studies[14]

Micro- and nanostructures have been found on many living creatures (algae, leaves, crustaceans, fishes, insects, and others). For example, some cicada (Fig. 3), planthopper and dragonfly species have a nanostructured wing surface showing antimicrobial effects.

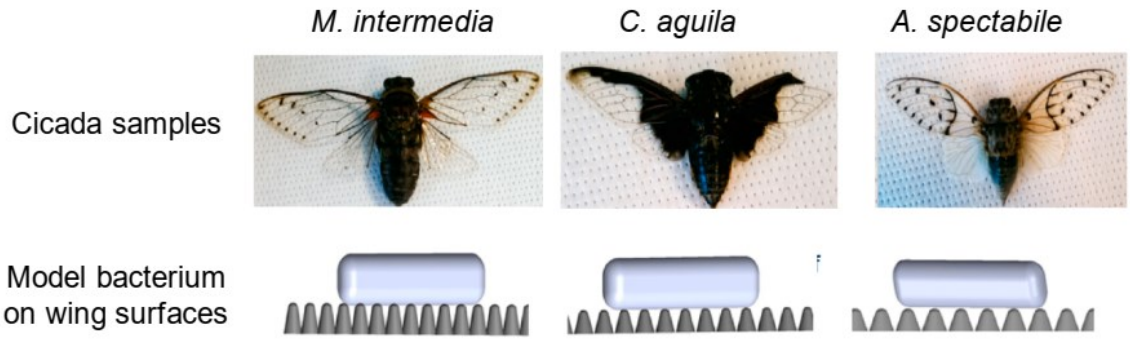

Figure 3: three species of cicada whose nanopatterned wings has antibacterial properties

The shark skin (Fig.4a) shows a good anti-biofouling micropattern (called "sharklet"); anti-biofouling surfaces are generally superhydrophobic, so that the adhesion of most of the species is harder; Bhushan et al. tried to create a hierarchical structured surface combining the microstructure present in the shark skin (anti-fouling), also present with a similar form in a butterfly, and lotus leaf (self-cleaning) effects, producing the so-called rice and butterfly wing effect[15].

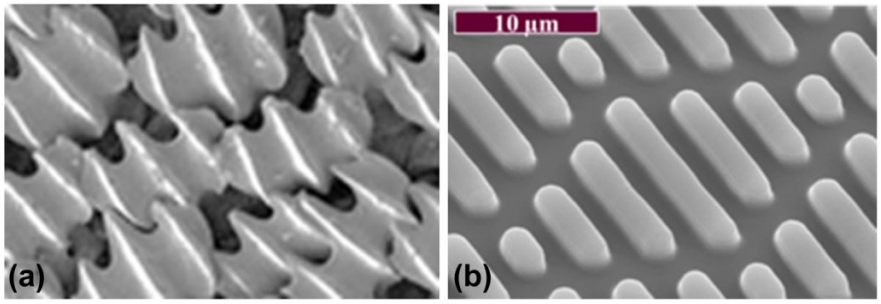

Figure 4: a), anti-fouling micropattern on shark skin; b), shark skin inspired micropattern[16]

Hierarchical structures are also present in nature and researchers are trying to mimic them aiming at achieving better performances with their properties[10,14,16, 17].

1.5.Polysulfone membranes

Polysulfone (PSF) belongs to the family of aromatic polysulfones (poly(sulfonylarylene)s), polymers with general formula: $(ArSO_2)_n$, where *Ar* represents a structure containing aromatic groups. The chemical structure of PSF is:

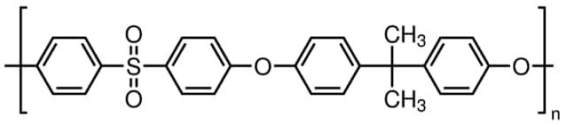

PSF is one of the most important polymer for membrane manufacturing, because of its chemical inertness, thermal stability, its mechanical resistance up to 170°C, as the glass transition temperature is in the 185-190°C range [18–20], and because of the possibility to obtain a wide range of membrane types for different applications. However, since PSF is hydrophobic, there is a tendency in biofilm formation. PSF membranes are currently used for water filtration and medical processes such as hemodialysis, osteointegration, and controlled drug release[5,21–23].

1.6. Aims of this work: micro- and nanopatterning of PSF electrospun mats

PSF porous membranes produced via electrospinning have been used in different applications so far; PSF nanofibers mats can be layered and treated to produce microporous membranes for microfiltration. Being the aim of the project reducing biofilm growth on PSF by developing an anti-biofouling solution, the approach adopted by this group is using micro- and nanostructures that can be found in nature.

The effect of antimicrobial natural nanopatterns on five cicada species' wings has been studied. Likewise, studies on the anti-biofouling efficiency of different micropatterns present on plants and animals could help the design of an artificial bioinspired micropattern that optimizes those properties.

This group's work aims at finding a scalable procedure to make performant PSF membranes with a hierarchically structured surface: an antimicrobial bioinspired nanopattern, similar to a nanopattern that can be found on the *Cicada Megapomponia Intermedia* 's wings and an anti-biofouling bioinspired micropattern[24].

In this work, a method for measuring the Water Contact Angle was developed that does not need a goniometer. The calibration of a tool to find a procedure for curing PEGDA and PPGDA, as materials used for anti-biofouling testing, was initiated. Studies on PSF single mats behavior under Hot Embossing conditions, together with micropatterning procedure tests attempts were made; also, experiments to find a procedure for nanopatterning of mats with promising results were conducted.

2. Theoretical background

2.1.Cross-linking of PEGDA and PPGDA

Cross-linking of PEGDA and PPGDA, biocompatible and water-soluble polymers, gives a three-dimensional polymer network of PEG (or PPG) forming a solid[25,26]. The cross-linking works using a photoinitiated polymerization, starting from the pre-polymerized species (Fig.5)[27,28]. Cross-linked PEG and PPG have been used by this group for replica molding of cicadas' wings nanopattern for anti-biofouling analysis. PEG primary molds and PPG secondary molds could be obtained because of the lower hydrophilicity of PPG than PEG: the difference in surface energy makes PEG from PPG demolding possible.

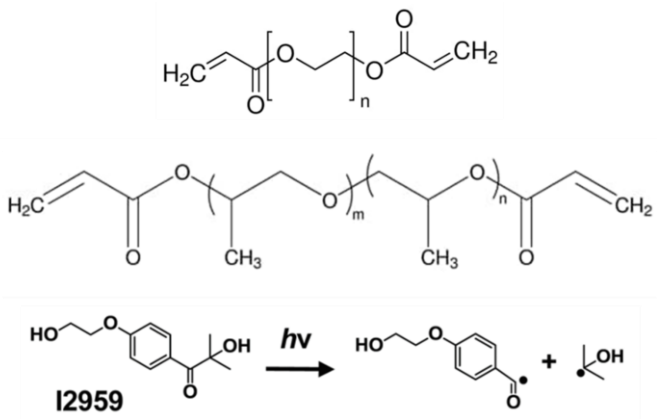

Figure 5: formula of PEGDA (above) and PPGDA (middle); mechanism of radical formation by irradiation of the photoinitiator Irgacure 2959 (below)

A photoinitiator is mixed with the polymer, containing acrylate groups; here, Irgacure 2959, was used as a biocompatible photoinitiator[29]. It forms benzoyl and hydroxyalkyl radicals under UV radiation.

Both the mechanism of photoactivated radical generation and further polymerization of PEGDA are shown in Fig.6; PPGDA undergoes a reaction with the same mechanism.

The two radicals react with the C=C bond in acrylate groups and consequently form two radical species, causing the initial step of radical polymerization (a new radical is generated), called initiation step (Fig.6b). Afterward, the newly formed radicals react with other acrylate groups (propagation step). The process ends when all the radicals are consumed (termination step)[30,31,32].

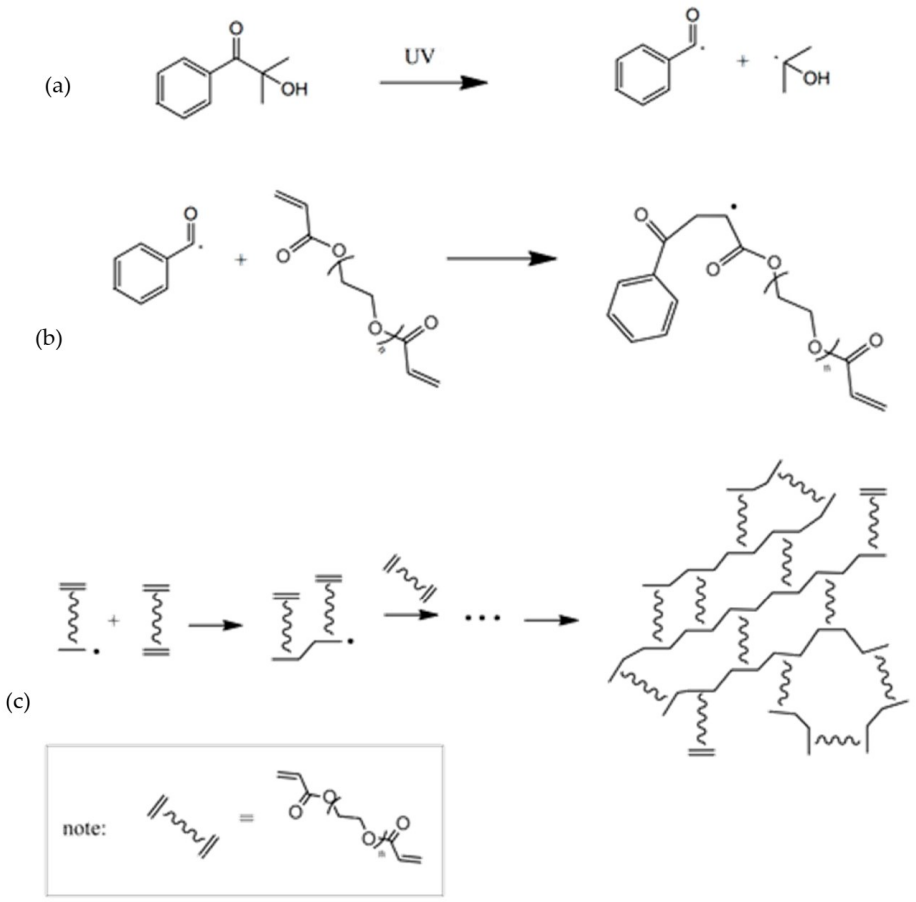

Figure 6: mechanism of PEGDA cross-linking: (a), initiation, (b), propagation (c), note[30]

For a fully cross-linked polymer, theoretically all the CC double bonds in acrylate groups should react during the propagation step and limit the reaction; if the termination step ends due to side recombination of radicals instead, the property of the cross-linked polymer might change.

2.2.Hot embossing

Research on micro/nano-manufacturing have been increasing in recent years, to meet the demand of industries for high-precision processing technologies; primarily the research on polymer manufacturing is increasing, as polymers can provide both electrical and thermal insulation, and biocompatibility. Compared to other technologies such as micro-injection molding, 3D printing and micro-casting electrospinning, Hot embossing (HE) is a promising technique as it works at relatively low pressures and temperatures and is suitable for the replica of polymer molds to both the micro- and nano-scale; hot embossed single-use components are widely used in microfluidic, biomedical, and micro-optical devices [33].

As follows, the classification of different HE types as well as the HE working principle through an explanation of the main steps, and a discussion on the effects of working parameters on the molds are outlined.

Classification of HE types

Three HE processes are mainly used, depending on the geometry of the mold and the support, mainly three HE processes can be distinguished: plate-to-plate (P2P), roll-to-plate (R2P), and roll-to-roll (R2R).

P2P-HE is the most commonly used approach to produce a nanopattern on a surface, because of its versatility (in this work, P2P HE was used); high aspect ratio (AR) micro and nanopatterns can be obtained with P2P; thanks to the employment of plasticizers and release agents, structures with AR up to 50 have been molded[34]. The polymer to be patterned is sandwiched between two plates one of which is the mold with the negative of the wanted pattern; the demolding step is non-destructive, and nanostructures are usually preserved. In this work, P2P HE was used.

R2P and R2R involve the usage of a roller and a plate (R2P), one of them being patterned, or two rollers (R2R). The polymer sheet flows between the rolls and gets the patterning; this process can also be coupled with UV lithography.

R2P and R2R approaches are faster and provide a wider surface that can be molded than in P2P; however, lower aspect ratios are achievable and besides, the demolding step must be controlled to keep the shape[35,36,37].

The operating principle of HE

A rigid nano or micro-patterned master template is used for imprinting a polymer to shape its surface: the master, the polymer, and a top plate are stacked in the embossing chamber and HE is obtained by increasing temperature and pressure for a certain amount of time. A setup for HE should provide a controllable heating system and applied pressure; vacuum inside the embossing chamber can offer further control (although not every HE experiment is run under vacuum): in some cases, depending on which polymer is employed, it leads to products with less defects.

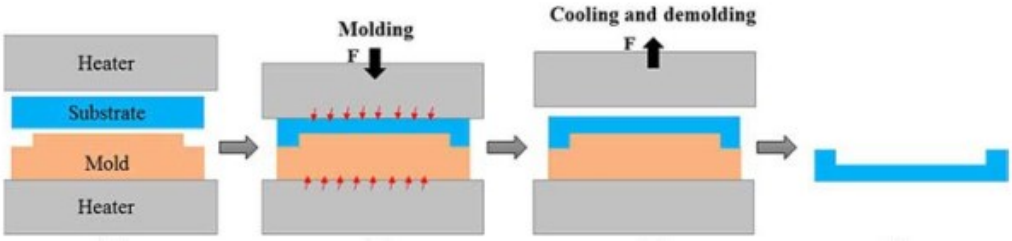

Figure 7: scheme of HE principle

The HE process can be divided into 3 main steps (Fig.7,8), even though further sub-steps are added in some cases:

1. T ramp

   The temperature inside the chamber is slowly raised to embossing temperature (T_E). T_E must be above the softening point of the polymer, which is the temperature at which it can flow under its own weight; the glass transition temperature (T_g), the chemical composition and the molecular weight of the molding polymer determine its softening point. The difference in temperature between T_g and ideal T_E usually depends on the polymer and on the pattern to be imprinted.

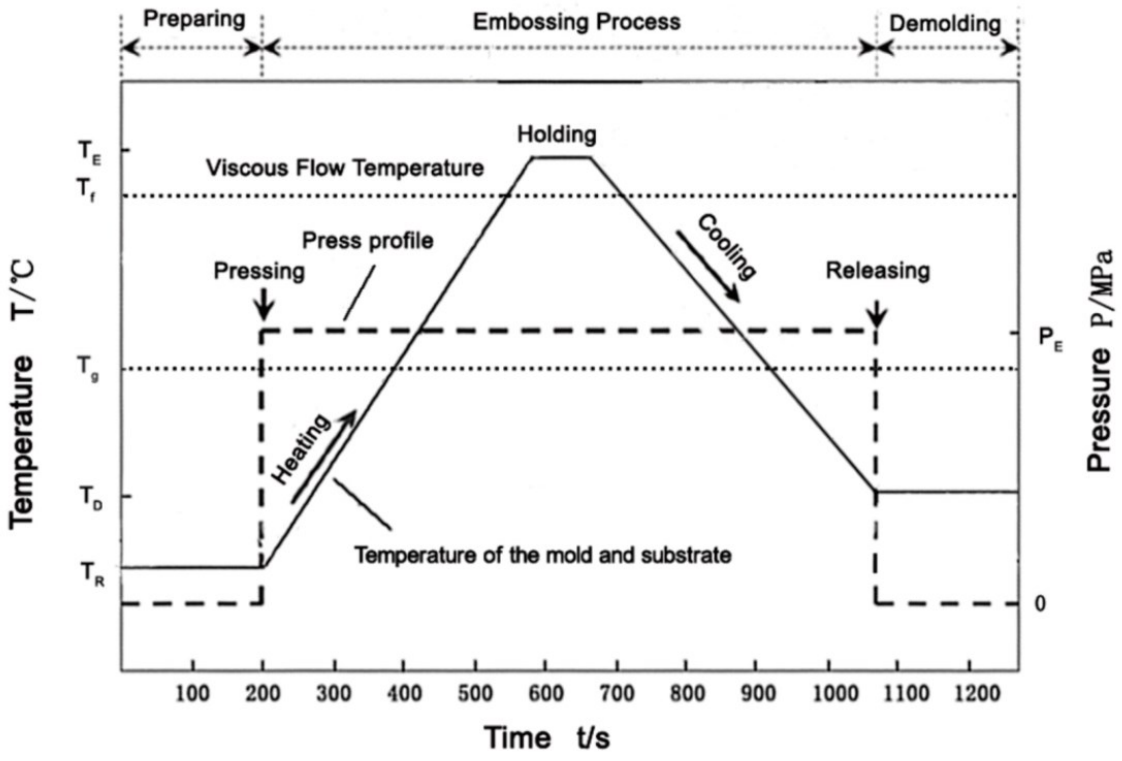

Figure 8: a diagram shows the HE steps: a T ramp, the molding step and the cooling step before demolding

2. Molding

   Once the sandwiched layers are heated, T_E is then held for a certain amount of time (embossing time), and pressure is evenly applied from above to allow shaping of the heated polymer. The use of high pressures could lead to excessive broadening of the molding polymer piece or deformations, and not necessarily to a better replica of the template.

3. Demolding

   Temperature is decreased down to the "demolding temperature" T_D which is a preset temperature below the T_g; demolding while the viscosity of the polymer is too high must

be avoided. The demolded imprinted polymer is surface-shaped, with residual mechanical stress[38,39].

Effects of the working parameters

The replicability of a HE process is very narrow, as accurately predicting the result of a HE is not trivial. Many studies have been conducted to find the effect of several parameters on the imprinting quality: working in vacuum, the nature of the polymer and the mold, the polymer's dimensions, thermodynamic conditions, shape and aspect ratio of the pattern, the preparation of the sample; among such parameters, most authors agree on embossing temperature (T_E), pressure (p_E) and embossing time being the most impactful parameters on the successfulness of a HE process.

It was found there is a correlation between all those parameters and a variety of defects in the samples, making it difficult to find a sweet spot: working without vacuum can cause some air to be trapped and deform the sample; thickness is not necessarily preserved; edges are hard to replicate accurately; non-homogeneity of the pattern alongside sample's sheets is common, due to the outward flow of the hot polymer that often brings to a non-symmetrical adhesion on the motif; therefore, deformation during the demolding step due to friction can occur. Thus, 3D modeling and advanced analysis is an effective way to improve results in this field that have been used by many groups so far[40–43].

2.3.Electrospinning

Electrospinning is a versatile technology for fabricating porous polymeric materials with tunable pore size, porosity, and morphology. At present, electrospun mats are produced in large volumes and employed in a broad range of applications: in air filtration (e.g. car filters), in food and agriculture industries, in cosmetics, and many other industries as a structural element; more so, the interest in the possible use of electrospun mats in more advanced fields intensified in the last decades, such as biomedicine but also electronics, catalysis, energy harvesting; among the array of applications on which research is currently active, membranes for water

filtration obtained via electrospinning have been produced and successfully tested before, bringing to promising results. This will be the main focus of the present work.

Principle of electrospinning

A droplet of a solution containing a polymer is charged as a consequence of an applied voltage; then, a jet forms and elongates; polymeric fibers are collected on a conductive surface as the solvent evaporates.

The main components of an electrospinner are: a high voltage power supply, a syringe pump, a spinneret (a needle), and a conductive collector (Fig.9).

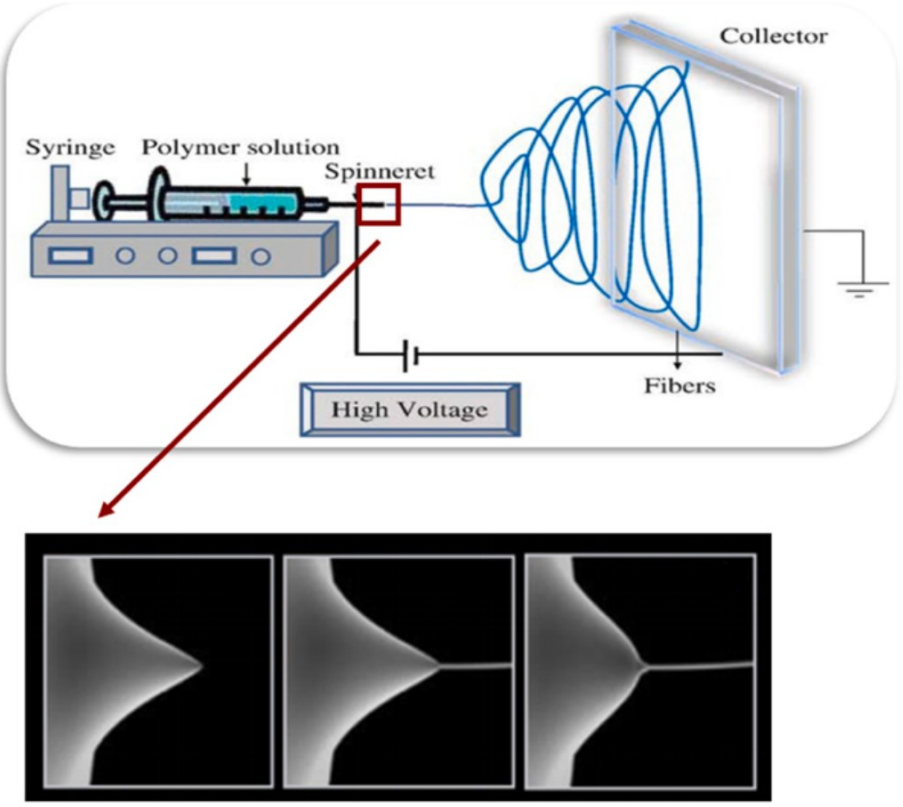

Figure 9: above, electrospinner simplified setup; below, the Taylor cone formation

The electrospinning process can be studied focusing separately on 4 steps:

1. Fluid charging

   A high voltage is applied between the spinneret and the collector; as a consequence, the liquid in the droplet pending on the spinneret undergoes charge separation; charges of the same sign of the spinneret start accumulating on the surface of the droplet. The droplet is deformed, because the charge separation generates a repulsion force which tends to elongate the droplet, whereas minimization of surface energy is reached if the surface is minimized (spherical shape).

2. Formation of the Taylor cone

   The voltage is increased up to a certain threshold (20-30 KV), at which the accumulation of the charges is high enough for the electrostatic repulsion to overcome the surface tension; to minimize electrostatic energy and surface free energy, the droplet ideally has a conical shape at this stage; if a viscous liquid is used, a higher voltage must be applied as the viscoelastic force of the liquid should also be taken into consideration; when a voltage above the threshold is applied, a jet is formed on the droplet. This phenomenon is called formation of the Taylor cone.

3. Stretching and thinning of the jet

   In the first part of the jet path, in the near-field region, it is accelerated by the voltage and follows a nearly straight line; afterwards, in the far-filed region, the jet curls and gets thinner following a random path, as an effect of several factors such as: surface tension, viscoelastic properties of the polymer, long wave perturbation propagating into the jet, electrostatic effects caused by the strong field and the charges on the solution.

4. Collection of the fibers

   The stretched jet solidifies and forms fibers, because of the evaporation of the solvent. When the fibers get in contact with the conductive collector, the charges are mostly dissipated; however, a measurable amount of them can remain on the surface of the

fibers. The buildup of these charges could reach the point to which further collection of the fibers is harder, because of the repulsive interaction between the mat and the elongating jet; this sets a limit to the maximum thickness of a mat, about 0,5-1 mm.

Because of the complexity of this process, it is understandable that many factors such as spinneret-to-collector distance, flux rate, polymer concentration, and voltage should be optimized to get a mat with the aimed features; for instance, a high voltage and a big distance between the spinneret and the collector would result in thinner fibers; a higher flux rate would instead result in thicker fibers; a wrong combination of parameters can easily lead to beading, the undesired accumulation of polymer within the fibers. Also, other parameters as humidity and temperature should be monitored, as they affect the morphology and dimension of the fibres[44–47].

2.4. Tests for Membrane for Water Filtration

Predictions about the behavior of membranes for their operating conditions can be supported by mechanical tests, analysis of porosity and pore size, and more specific tests such as flux tests, rejection tests, and Water Contact Angle (WCA) test.

2.4.1. *Water Contact angle test*

Membranes for WF could be either hydrophobic like PSF or hydrophilic (also zwitterionic membranes have been produced). There is often a correlation between wettability and durability, and fouling susceptibility of membranes, so the Water Contact Angle (WCA) is usually measured. The contact angle (CA) is defined as the angle between the solid surface plane and the tangent to the liquid surface plotted at the point of contact between the three phases. It depends on the surface tensions of air-support, air-water, and water-support interfaces; to describe a droplet on an ideal smooth surface (Fig.10), the Young's equation is commonly used:

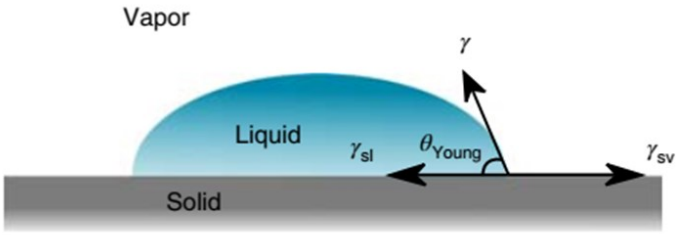

$$\cos\theta_{\text{Young}} = \frac{\gamma_{\text{sv}} - \gamma_{\text{sl}}}{\gamma}$$

Figure 10: scheme of a liquid droplet on a perfectly smooth surface; Young's equation

However, PSF micro- and nanostructured membranes clearly cannot be described by this model (Fig.11). A droplet interacting with a textured surface so that there is air trapped underneath can be described by the Cassie-Baxter model, according to which the CA should raise when compared to the smooth surface model based on Young's equation. Also surface roughness plays a role in the resulting CA: according to the Wenzel model, a rough surface can lower the CA because of the higher water-support surface interface available. Whether the Wenzel or the Cassie-Baxter models should be used depends on the system.

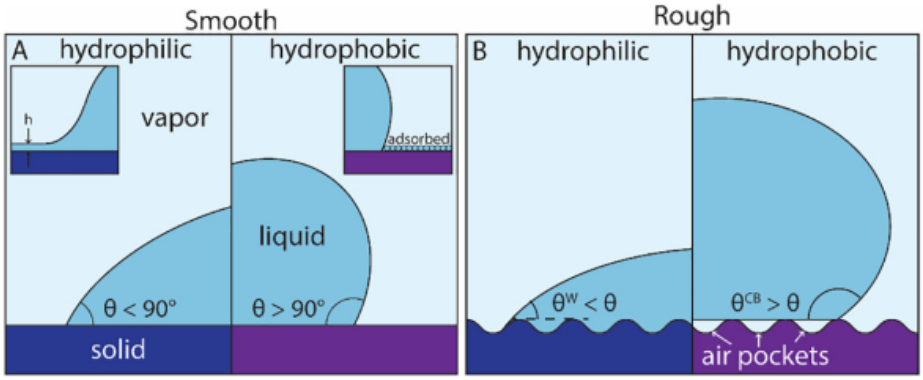

Figure 11: liquid droplet on hydrophilic and hydrophobic smooth surfaces described by the Young's equation (left); liquid droplet on a hydrophilic rough surface, described by Wenzel model, and hydrophobic rough surface, described by the Cassie-Baxter model

A Contact Angle goniometer is generally used, whose setup is represented in Fig.12.

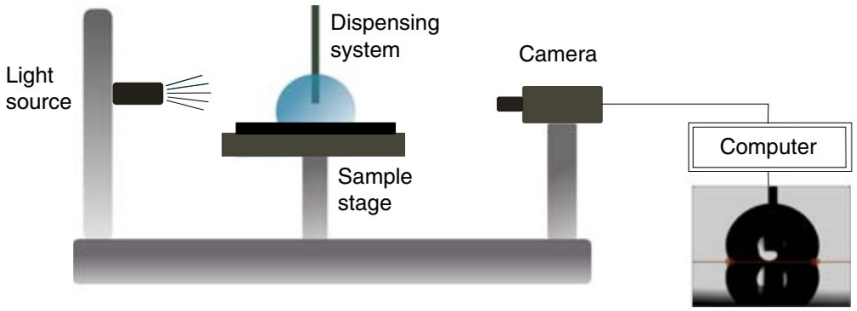

Figure 12: WCA goniometer setup

A droplet is dispensed from a syringe (dispensing system) onto the surface to analyze, while a camera takes images of the droplet; the camera should have a good timing control and high time sensitivity; the axis of its lens must be horizontally aligned with the specimen, in order to avoid inaccurate measures due to parallax error; a light bulb pointed towards the camera increases the contrast in the image, making analysis easier and leading to more precise results.

Gravity affects the droplet shape, so its weight must be kept constant for every measure; also uncontrolled deposition could lead to different results, so the dispenser must be oriented perpendicularly to the surface. A volume in the 1-10 µl range is usually used for WCA analysis[48–52].

The WCA for porous PSF was measured by members of this group, reporting a range of results, 79.5 to 102.5.

2.4.2. *Mechanical tests*

Several tests such as punch test, bursting test, tear test, uniaxial tensile test and others can be used to evaluate mechanical stability of a membrane, depending on different parameters to be studied for different applications. Among them, the uniaxial tensile test is more commonly used, as it allows to get stress-strain diagrams. These curves (Fig.13) describe the behavior of a material while a tensile stress is applied; the formula that describes the curves in the elastic (linear) region is

$$\sigma = E\varepsilon$$

where E is the Young's modulus, σ is the applied stress, and $\varepsilon = \frac{\Delta l}{l}$ the corresponding elongation. The Young modulus gives information on the elastic behavior of the material; the yield stress represents the stress value at which the material's behavior switches from elastic to plastic; the maximum stress that the material can withstand before breakage is called tensile strength.

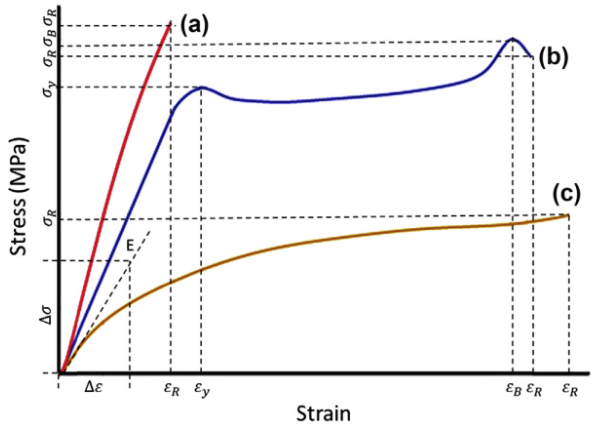

Figure 13: typical stress-strain curves for (a) brittle materials, (b) ductile materials, and (c) rubber-like materials.

This test is usually carried out with a universal testing machine: the opposite ends of a specimen of standard dimensions are gripped, and a stress ramp is applied with a predetermined speed until a certain value is reached or to failure. A stress-strain curve is built out of this tests by monitoring the percentage elongation of the specimen while the stress is applied[53–55].

2.4.3. *Flux test*

The flux test is for finding the volume *V* of the water that passes through the membrane per area (*A*) and time (*t*) unit; the flux *J* is described by the equation

$$J = \frac{V}{A \times t} \quad ; \quad [J] = \mathrm{L\ hr^{-1}\ m^{-2}}$$

Flux tests have been previously conducted by members of this group using a dead-end filtration setup, whose mechanism is shown in Fig. 14; on one side of the testing membrane a water inflow feed is forced perpendicularly to the membrane and kept constant by applying a certain pressure; the amount of water that passes through the membrane after an arbitrary amount of time is measured; by knowing the surface of the membrane it is possible to calculate the flux. This method is commonly used on small scales in laboratories to measure the water flux.

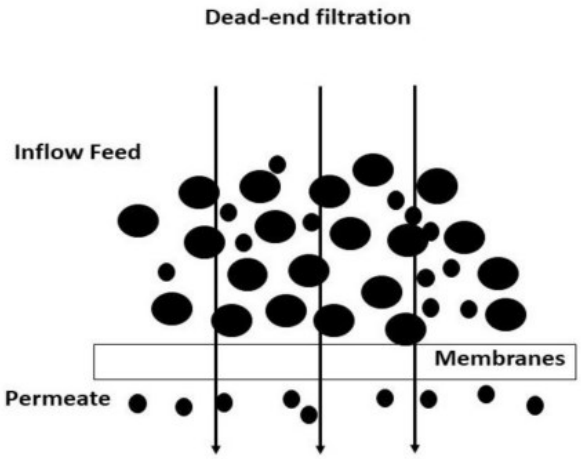

Figure 14: Scheme of the dead-end filtration

The flux has been measured by members of this group in the past years; a pressure difference of 1 bar between the sides of different membranes of known size was applied; the flux was found to be in the 19-22 $L*m^{-1}\ hr^{-1}$ range.

2.4.4. *Rejection test*

The rejection test indicates which class of pollutants a membrane is able to filter out; thus, it determines whether a membrane is possibly suitable for MF, UF, NF, or RO.

To discover which size classes of particles are retained and which ones pass through the membrane, different samples of water are prepared with ink-coated beads of controlled size; each sample contains a pre-set concentration of beads of a given monodispersed size; as for the

flux test, a pressure is applied to let the water pass through the membrane; after every test, the permeate is analyzed with UV-Vis spectrometry in order to check the presence of the beads.

The percentage rejection can be determined using the equation

$$R = (1 - C_p / C_f) \, x \, 100$$

Where R is the rejection (%); C_p is the concentration of the permeate solution and C_f is the concentration of the feed solution. Previous studies of this group found that beads of 2.1 μm diameter were filtered out from electrospun PSF membranes [56–58].

2.4.5. *Porosity and pore size*

Information on membranes' pores gives a better understanding of other parameters such as the flux rate and the rejected species; many methods for measuring porosity, pore size, and pore size distribution (PSD) are available. Depending on the material to be analyzed and the size of the pores, the best technique to use might vary. There are direct and indirect methods: direct methods include microscopies; they require mathematical model-based analysis and are usually time-consuming; indirect methods use some theoretical basis to convert measurable parameters into pore size and other information; they usually less time than direct methods, but not always provide detailed information about the size of the pores and PSD. Indirect methods such as Gas Adsorption Desorption (GAD), Permporometry, Evapoporometry (EP), Liquid-Displacement Porosimetry (LDP), Mercury intrusion Porosimetry (HgP) and thermoporometry are techniques for determining porosity and in some cases information about the pores size.

The HgP method is often used: a porous sample is placed in a chamber, then vacuum is pulled. Afterwards, liquid mercury is poured and a high pressure is applied; at this point, pores as small as approximately 0.003 μm in diameter are filled with mercury. Thanks to pressure-volume curves, a measure of porosity can be obtained this way [59–63].

2.5.Characterization techniques

2.5.1. FTIR-ATR

IR spectroscopy is a widely used technique in chemistry, biology, and biomedicine as it allows qualitative analysis of many chemical species of different sizes, ranging from small molecules to high molecular weight polymers and biomolecules. Different chemical bonds absorb IR light with selective wavelengths that are separate enough from each other's in the IR region depending on the strength of such bonds; that is why even organic molecules with a high molecular weight and characteristics bond alongside their structure (functional groups) can be detected this way.

A functional group can be identified in IR spectrum as it absorbs light within a band in this region. Absorption peaks are associated with the fundamental vibrations of a functional group: the overall motion of a molecule can be described as the combination of several independent vibrations with specific frequencies called normal modes; light with the same frequency of a normal mode is absorbed by the molecule and generate a vibrational transition if it causes the molecule to change its dipole moment. A normal mode showing this property is said IR active and can be detected; a species can be identified with IR spectroscopy thanks to its IR active normal modes whose bands and absorption intensities are tabled.

A typical IR spectrum is a wavenumber vs Transmittance plot. The wavenumber ν ($cm^{-}1$) is the reciprocal of the wavelength λ (cm). In order to probe the IR absorption, in IR spectroscopy a laser passes through a sample and its frequency is scanned over the range of interest, which is usually 4000-500 cm^{-1}. Since scanning used to be a very time-consuming part of the process, Fourier Transform (FT) IR followed first-generation IR spectroscopies.

Fourier transform is a mathematical tool that permits the re-arranging of a function as the sum of simpler sinusoidal functions with certain frequencies and amplitudes. In FTIR, this tool makes it possible to bypass the wavelength scanning step, as all the frequencies are analyzed at once. However, a (faster) scanning step is required: FTIR spectrometers work with the Michelson interferometer (Fig.15):

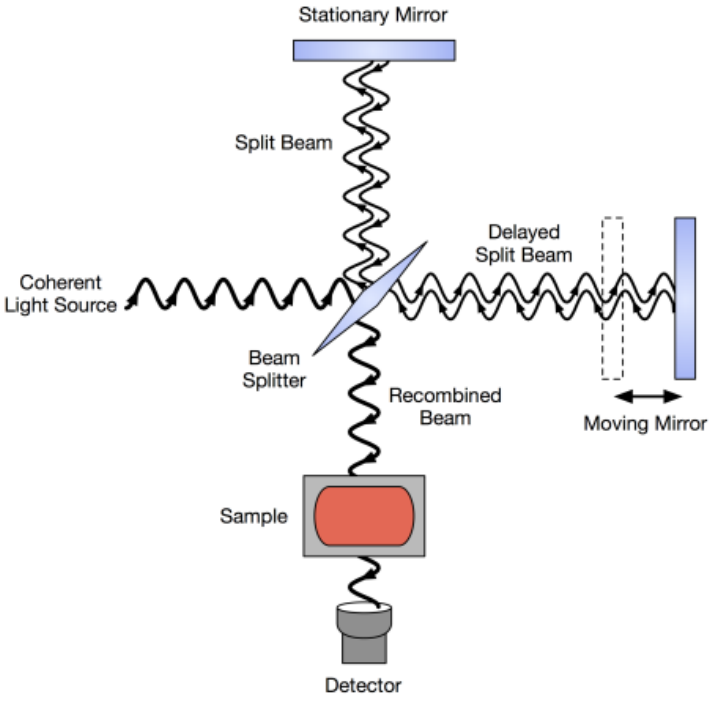

Figure 15: Michelson interferometer scheme

A coherent polychromatic light beam passes through a beam splitter, to be split as shown; half of the beam is reflected by the beam splitter, then reflected by the stationary mirror (top) and is kept coherent by constructive interference; half of the incident beam goes through the beam splitter and interferes constructively or destructively depending on the position of the moving mirror. The beam resulting from the recombination of the coherent beam and the varying beam passes through the sample. Intensity is a function of the optical path difference, thus of the position of the moving mirror; an interferogram obtained in this way contains the spectral information: all the frequencies are analyzed at once thanks to FT. The resolution is usually around 4 cm^{-1} and depends on the length of the path of the moving mirror.

Not every sample can be analyzed with normal FTIR; water molecule bonds absorb IR radiation, so molecules in aqueous solutions can't be probed; Solid samples must be crushed and mixed with KBr (invisible in the wavenumbers range of interest) to avoid internal reflection.

Attenuated Total Reflection FTIR is a technique that involves the usage of a high refractive index diamond, it is based on total internal reflection phenomenon. As shown in Fig.16, light passes through the diamond and is reflected on its top, then follows a symmetrical path and is collected by a detector.

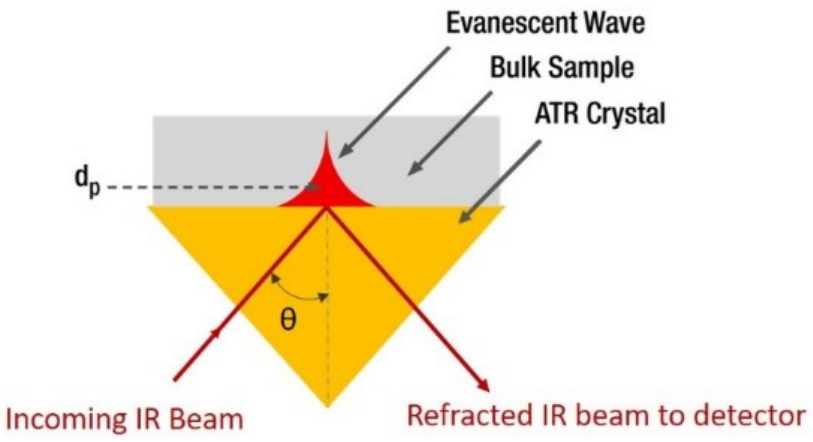

Figure 16: scheme of ATR configuration (image taken from Aurora Pro Sci website, link 1)

Even if the internal reflection is total, an evanescent wave forms beyond the border of the diamond and is attenuated by absorption within a few microns (0,2-3 μm), depending on what is the local environment: by placing a sample on the top of the diamond, it is then possible to deduce which frequencies of the light were absorbed.

This technique requires almost no sample preparation and it's non-destructive. It analyzes only its surface within 1 μm in depth. The solution can be analyzed as well because the signal is weak enough compared to normal FTIR [64,65,66].

2.5.2. Scanning Electron Microscopy

Scanning electron microscopes (SEM) have higher resolution than optical microscopes thanks to the employment of electrons instead of light. An electron beam interacts with the sample and generates secondary electrons (SE) and backscattered electrons (BSE); two detectors collect SE and BSE and software builds up an image. The structure of a SEM is reported in Fig.17:

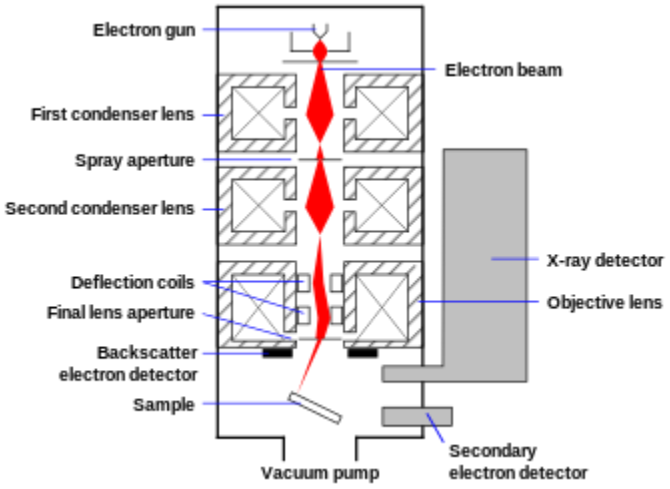

Figure 17: scheme of a SEM instrument

The basic principles of SEM operation will be briefly discussed straightforwardly by explaining each step of the electrons' path from the source to the detector.

Source

An electron gun controls the emission of the electrons. A simple and commonly used source is a thermionic electron gun with a V-shaped tungsten filament; a current flows through the filament for electrons being liberated by thermionic emission and a bias is applied to accelerate them down the electron column (high vacuum is needed all across the instrument body). Electrons emitted from different portions of the tungsten tip are directed toward different directions; this effect called chromatic aberration is minimized by using limiting apertures.

Field emission guns emit electrons without heating the tip; field emission is based on tunneling effect: structured Mo, Si or C nanotips allow electrons emission when the applied voltage is higher than their working function. A beam generated by a field emission gun has a higher current and less scattering; thus, a better resolution is achieved.

Column

Electromagnetic lenses are the main optical components in the column, they shape and focus the electron beam. Condenser lenses restrict the diameter of the beam; the objective lens focuses the beam onto the surface of the specimen. Minimization of astigmatism and spherical aberration can be optimized thanks to these optical elements.

Interaction with the sample

Incident electrons interact with the sample in a number of ways and likewise produce different signals; among them, Secondary electrons (SE) and Backscattered electrons (BSE) are analyzed to build up an image of the sample:

i. SEs are released from atoms in the sample as a consequence of the collision of the beam with outer shells; only SEs coming from surface atoms from up to a 10 nm depth can be collected by the SE detector, as deeper SEs do not have enough energy to escape the sample; most SEs have a kinetic energy within a 1-10 eV range; they mainly provide topological information.
ii. BSEs are electrons that have been scattered either elastically or inelastically as a result of interactions with nuclei; BSEs have higher energies than SEs (more than 100 eV), escape the sample from up to 1 μm depth, and are sensitive to composition: electrons are more likely to be backscattered by high atomic number elements, that will appear brighter than elements of a lower atomic number[67,68].

2.5.3. Atomic Force Microscope

Scanning Probe Microscopy (SPM) allows getting images by means of a probe scanning a specimen's surface and a signal which is unambiguously related to a probe-sample interaction. A feedback system instructs the probe how to move up and down while scanning the specimen; it plays a key role in this technology.

The Atomic Force Microscopy (AFM) is a type of SPM that uses Van Der Waal's forces as probe-sample interaction. The probe, called cantilever, is composed of a spring ending with a tip. During an AFM experiment, the probe is scanning a sample horizontally while being kept above the surface to a constant height or interaction force by the feedback system. Once the tip approaches the sample, any tip-sample interaction would cause the cantilever spring to deflect; such deflection is measured by means of a laser which is reflected on the cantilever itself and detected by a photodiode. The cantilever deflection results in a change of signal recorded by the detector (Fig.18). This process provides topographic information on the sample surface since every point of the surface being analyzed is defined with atomic resolution.

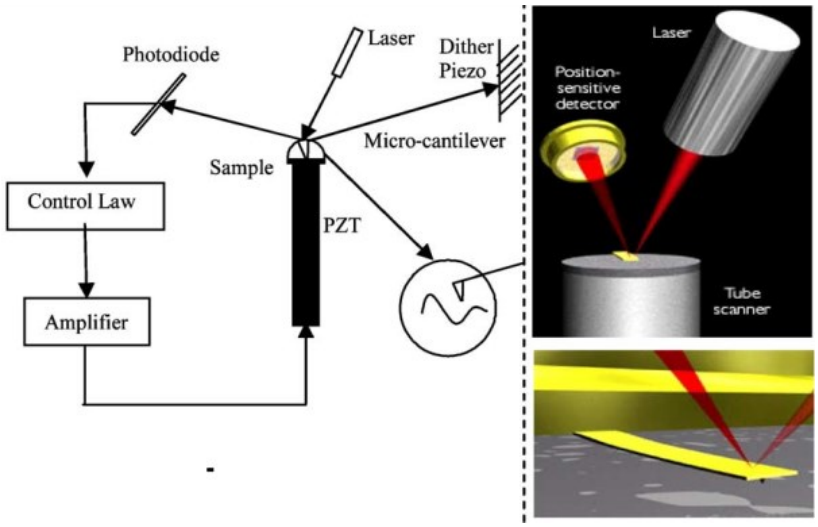

Figure 18: scheme of an operating AFM

The Lennard-Jones potential plot shows that interaction forces between two atoms/molecules can be attractive (Van Der Waal's) or repulsive (Pauli repulsion) depending on the distance, that

is why mainly three modes to which AFM can work were developed based on the distance between the tip and the sample: Non-Contact mode (NC), Contact mode (C), and Tapping mode (T).

While the Contact mode is used, the tip is kept in contact with the sample, the interaction force is kept constant by the feedback system, and the z-axis shifts are measured. Capillary and mechanical forces (the shear of the tip itself) must be considered; this is a risky method to use as both the sample and the tip could be damaged.

The NC approach is safer and suitable for soft samples, as the probe is working without any contact with the sample. The attractive forces between the tip and the samples are detected through a change in amplitude, frequency, or phase of the oscillation. Typically a fluid layer is formed on samples, which makes it difficult to exploit weak attractive forces.

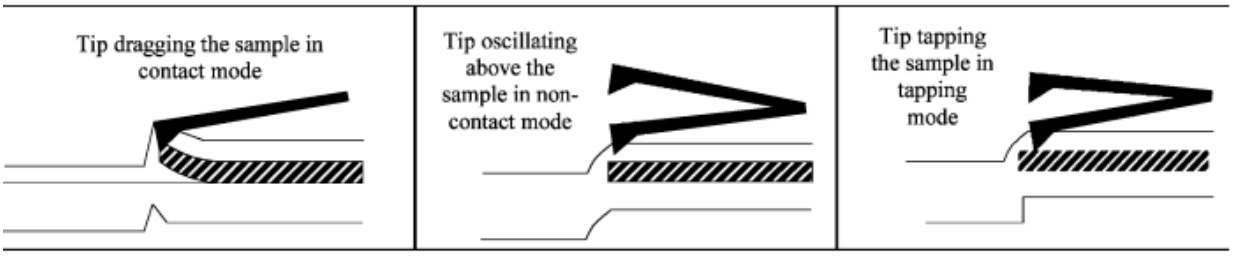

Figure 19: schemes of contact mode (left), non-contact mode (middle), and tapping mode (right)

The tapping approach works differently: a piezoelectric material is connected to the cantilever to give it a pre-set frequency at or near its natural frequency of oscillation, which depends on what the cantilever is made of and on its geometry (also the feedback system works thanks to the piezoelectric piece). The range of motion of the oscillating tip lies in both the attractive and the repulsive regions; the tip is mostly not in contact with the sample, but it impacts its surface and feels a repulsive force for a small amount of time (Fig.19). Thanks to this operating system, a high sensitivity is reached while bypassing the risks of working in Contact mode.

Among SPMs, AFM provides the chance to analyze a wide variety of sample compositions (metals, semiconductor, polymers, biological materials); there are virtually no limits to the type

of material of which an AFM image can be taken. Instead, the main problems with this technique are related to the probe defects and to a fluid thin layer that can easily form on the samples to be analyzed [69,70].

3. Materials and methods

3.1.The CNI-NILT tool

The CNI (Compact Nanoimprint) was purchased from NIL Technology (Fig.20). It is a versatile desktop tool for replicating micro- and nanostructures from a master to a substrate; both thermal or UV imprint and hot embossing can be performed with this instrument.

Figure 20: the Compact NanoImprint tool

A desktop provided by the same company allows to automate experiments by controlling step-by-step thermodynamic conditions and UV exposure inside the insulating chamber. The stamp and substrate are loaded manually. Three modules regulate pressure, temperature, and UV radiation respectively:

1. A pressure from 0.3 to 10 bar with 0.1 accuracy can be applied thanks to a swelling membrane placed on the top lid so that a force is applied downward; pulling vacuum in the chamber is also possible.

2. The bottom plate in the chamber is the heating element and stamp carrier; it allows heating up to 200 °C and cooling down to 50°C with control of ±1°C.
3. A UV lamp is placed beyond the membrane (which is non-absorbing UV), its power can be tuned from 10% to 100%. The lamp is a LED with an optical power of 1650 mW and a peak of absorption of 365 nm.

All the working parameters can be used simultaneously.

3.2.UV-Curing of PEGDA and PPGDA

Solution preparation

Before preparing a solution of either PEGDA or PPGDA, a glass vial was covered with foil, as the Irgacure 2959 should be protected from light as possible. 1% Irgacure 2959 was weighed in the glass Vial and dissolved with 2-3 drops of acetone; the smallest amount possible should be used to avoid slowing subsequent evaporation. The glass vial was filled with 99:1 Irgacure 2959 to PEGDA or PPGDA ratio. A piece of foil was used to replace the lid of the glass vial and punctured to let the dissolved acetone evaporate from the solution; the vial was then left under vacuum for 2 hours. Finally, the solution was used for cross-linking or stored using the lid.

Sample preparation

Two equal height PDMS cuts were rinsed with ethanol and placed on a TOPAS slab, approximately 5 mm from each other; then, another TOPAS slab was put on the top; the structure was wrapped with tape on the left and on the right side as shown in Fig.21;

Figure 21: the structure for a sample before injecting the cross-linking solution

The sample structure must be examined: to prevent leaking, the PDMS cuts should not be able to move easily; there should not be any space between the PDMS cuts and the TOPAS wall; if present, sharp edges should be covered with tape to prevent the internal membrane in the tool from undesired breakage. Using a micropipette, some PEGDA or PPGDA solution was injected into the cavity between the TOPAS and PDMS walls; Interruptions during the injection would cause bubbles formation. The sample could then be put into the chamber for UV curing.

3.3.Curing of Polydimethylsiloxane

Polydimethylsiloxane (PDMS) slabs were prepared for two purposes: as a structural element for sample preparation in UV curing of PEGDA and PPGDA; to be molded and used as a micropatterning master.

PMDS slabs were obtained using the Sylgard 184 elastomer, which is supplied as a two liquid component kit: a vinyl terminated Silicone and a “curing agent” to be used with a 1:10 ratio cross-linker to the elastomer, provided by the company Sigma-Aldrich. The mixture was cast on a mold and cured for 2 hours at 160 °C. A scalpel was used to cut pieces of different sizes (Fig.22).

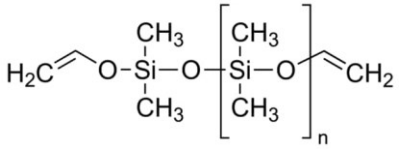

A PDMS micropatterned master was obtained by casting the mixture onto a Polylactic acid (PLA)-based 3D printed negative mold (fabricated by a collaborator), then cured at room temperature for 3 days and demolded. Smaller cuts of the master were taken for imprinting of the microstructure.

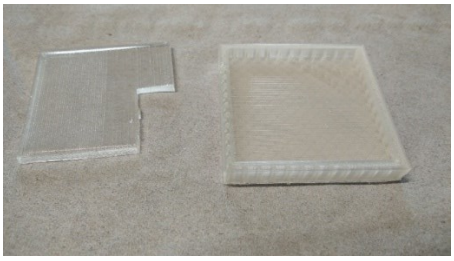

Figure 22: PLA 3D printed micropattern piece (right side), and the demolded PDMS piece after curing (left side)

3.4.Silanization of the Silicon Master

Firstly, the master was cleaned from organic residues with piranha solution at 80 °C for 45 minutes, then washed and dried. OH groups should form on the Si surface. Secondly, vapour deposition of Trichloro(1H,1H,2H,2H-perfluoro-octyl)silane (PFOCTS) was carried out[71], as shown in Fig.23:

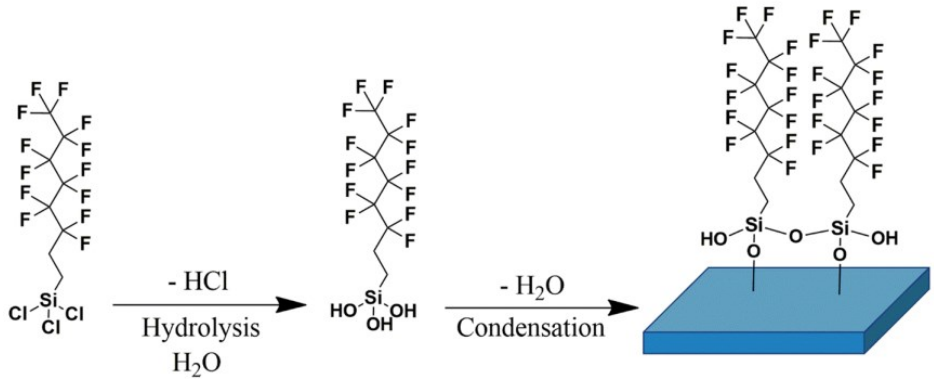

Figure 23: mechanism of the formation of a self-assembled monolayer of PFOCTS

a handmade foil boat was placed in a vacuum chamber, then the master and a small vial have been placed in the boat (Fig.24);

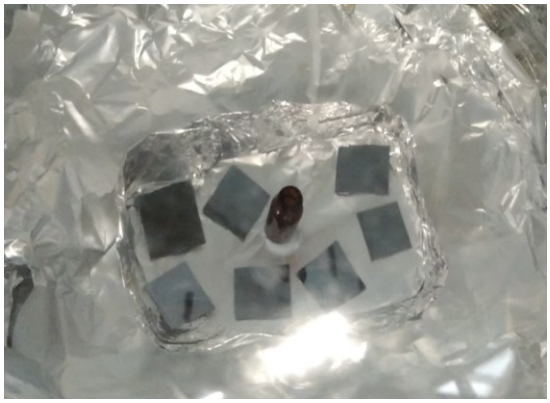

Figure 24: Chemical deposition of PFOCTS: a tin boat inside a vacuum chamber with a small vial and 7 silicon slabs

2/3 droplets of the molecule were put in the vial and vacuum was pulled for 3 hours. A hydrophobic self-assembled monolayer of the molecule forms on the surface (Fig.25), thanks to the presence of pendent OH groups on the silicon master. The master was rinsed with toluene and dried after deposition, to remove excess of the self-assembling molecule.

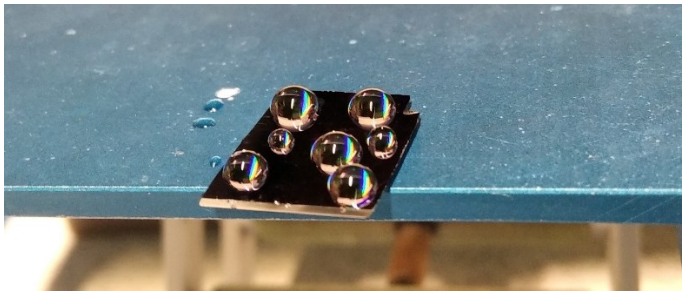

Figure 25: droplets of water on the silanized silicon master

3.5.Micropatterning

The PLA 3D printed master for micropatterning the membranes was produced; a PDMS negative mold was obtained by curing liquid PDMS after casting onto the master; the demolded PDMS stamp has been used to engrave the pattern to PSF mats via HE.

The CNI tool was used for this purpose. From the bottom to the top layer respectively, the PDMS master, a piece of mat, a Si top plate, and a Teflon protective sheet were sandwiched (Fig.26).

layering of the components for HE samples: the micropatter, a mat, a silicon slab, a teflon sheet

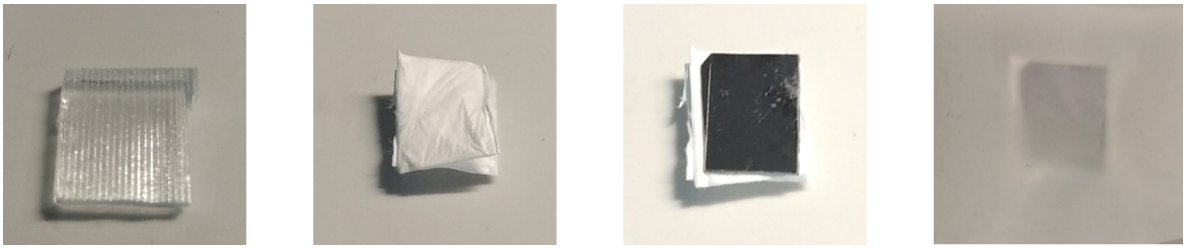

Figure 26: layering of the components for HE samples: the micropatter, a mat, a silicon slab, a teflon sheet

After closing the chamber properly, the temperature, the pressure, and the embossing time are chosen on the software before running the recipe.

3.6.Electrospinning

PSF mats were produced via electrospinning following a standard procedure, previously tested and compiled by the present group. This standard procedure works with horizontal configuration.

A mixture of 20% acetone and 80% dimethylacetamide was used as a solvent. A solution of 23% weight PSF was prepared, put in a beaker with an anchor magnet, covered with parafilm, and let stir overnight; Different weights led to beading (formation of globules) in the fibers (as demonstrated by the group previously).

A syringe was used to feed the electrospinner, was placed in a specific compartment of the module structure. A software controls the flow rate; a flow rate of 5 ml/h was set. The syringe pushes the solution in a tubing and then into a 5 needles support connected to the tubing; the support is placed on a structure with gaskets to minimize its motion (Fig. 27).

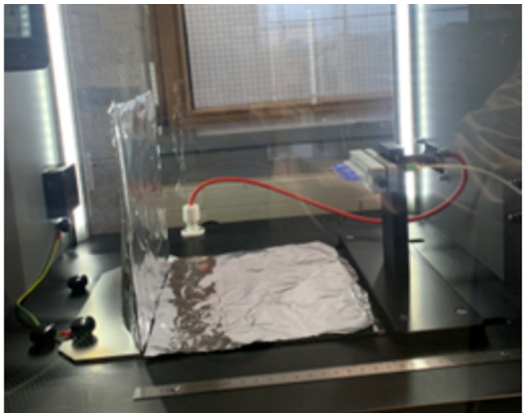

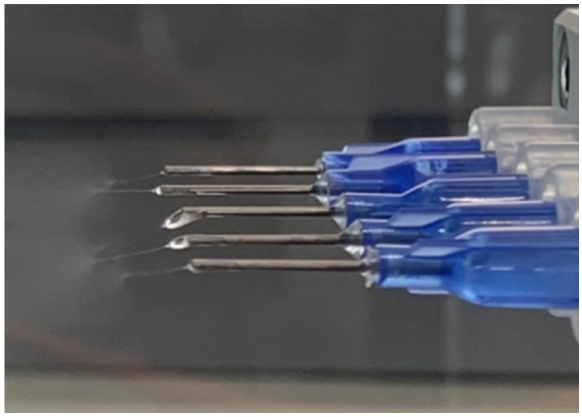

Figure 27: electrospinner, horizontal configuration (left); multineedle tool, detail (right)

The applied voltage is around 20V, and must be monitored constantly and often adjusted, as the Taylor cone shape is a narrow equilibrium condition. Despite the chamber insulation system, the humidity was varying in the 30-40% range.

Figure 28: an electrospun mat obtained with the described standard procedure

A mat forms after 1h electrospinning (Fig 28). All the components must be carefully washed with acetone after each use to prevent the PSF residues from clogging the tubing and the needles.

3.7.Contact angle of a water droplet on the Silicon Master

CA measurement of a water droplet on a membrane surface is an indicator of the hydrophobicity of the membrane; thus, a procedure for measuring the contact angle (CA) of membranes was developed using the electrospinning apparatus available in the lab; the master was used for testing and its hydrophobicity after silanization was verified this way; this method could be helpful for membrane analysis in future research.

The camera was oriented towards the end of the needle and focused on it; the master was placed on the stand (Fig. 29); the stability of the structure was checked and the master's positioning deviation from horizontality was minimized.

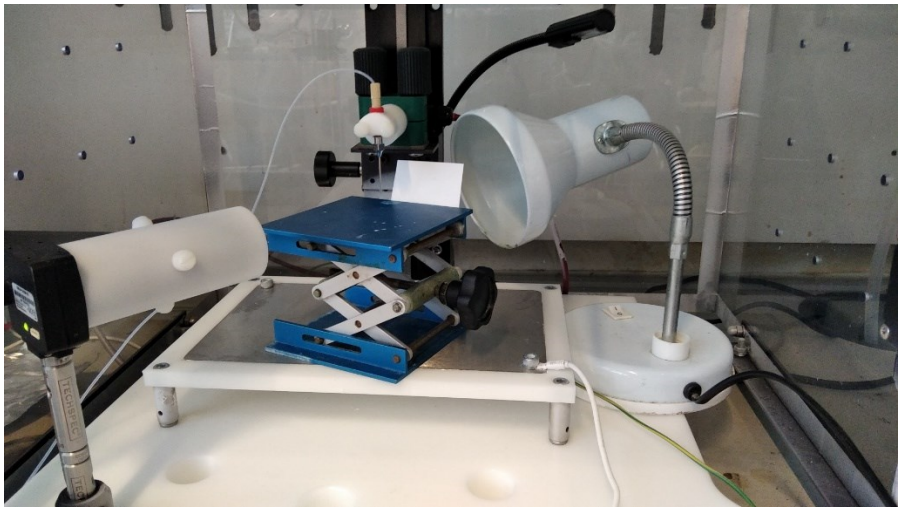

Figure 29: WCA analysis setup using the electrospinner

Placing the master without losing image definition needs great care: it was found the best way was letting one edge of the master lay on the same line linking the electrospinner needle and the camera lens axis; the two sides of the master are focused in one point each in this way, and the horizontal line connecting them in a picture can be used as a baseline.

A syringe was filled with deionized water and assembled in the electrospinning apparatus. The camera control program allows taking multiple images in a row with a 1ms control on time shift,

so the CA of every sample can be estimated consistently as after the droplet falls from the needle onto the master a picture is taken after a certain amount of time and can be selected.

The analysis of the contact angle was carried out using a free plugin for ImageJ, Low Bond Asymmetric Drop Shape Analysis (LB-ADSA). By setting the parameters as shown in Fig.30, it was manually possible to define the shape of the droplet and the software analyzes the contact angle automatically.

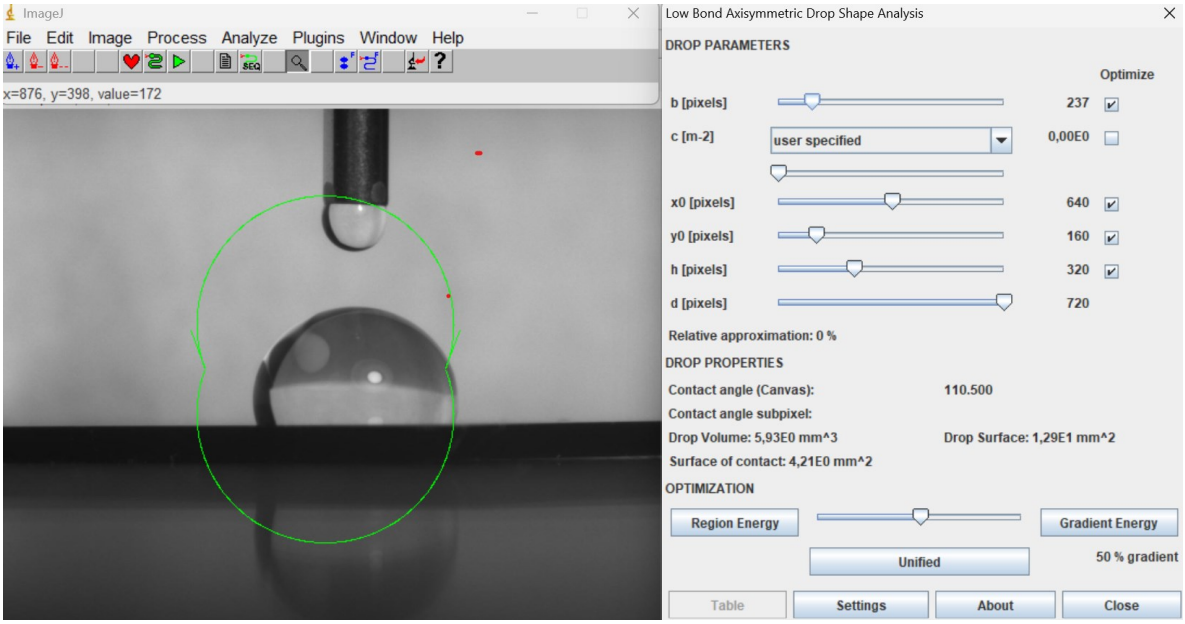

Figure 30: view of the LB-ADSA software analysis

3.8.Characterization techniques

The "Hitachi S-3400 VP" SEM, the Zeiss Plus-SEM Field Emission SEM, and The Hitachi S5500 Field Emission SEM were used; The samples were mounted on 15 mm diameter stubs with Carbon paste or carbon tape; all the PSF samples were gold-coated to avoid charge buildup. The "Bruker Dimension Icon" AFM with ScanAsyst mode and the "Perkin Elmer Spectrum Two FTIR-ATR" were used.

3.9.Experimental

Each of the listed chemicals was purchased by the company *Sigma Aldrich*: for the CNI tool UV cured PEG and PPG, PEGDA (polyethylene glycol diacrylate, Mn~575) and PPGDA (poly propylene glycol diacrylate, Mn~800); the photoinitiator was Irgacure 2959 (2-Hydroxy-4′-(2-hydroxyethoxy)-2- methylpropiophenone). The Sylgard 184 elastomer and cross-linker used to make PDMS (polydimethylsiloxane) slabs; the self-assembling species used to deposit a monolayer on the silicon master was Trichloro (1H,1H,2H,2H-perfluoro-octyl) silane, and toluene was used for rinsing. PSF tablets (MM=35000 Da), Dmac (dimethylacetmide) and acetone were used to make the solution to be electrospun.

4. Results and discussions

4.1.Contact angle of a water droplet on the Silicon Master

The contact angle of the nanopatterned master was measured after cleaning with piranha solution and after deposition of the hydrophobic coating (Fig.31). For every measure, a picture that had been taken 2 seconds after the drop fell on the master was chosen. This test was carried out to test hydrophobicity and investigate on the limits of this method for accurate WCA analysis.

Three measurements were taken to test the wettability of the master; further experiments aiming at studying this method applicability for more accurate analysis of WCA were not conducted, as the setup did not allow analysis of droplets smaller than 16 µl.

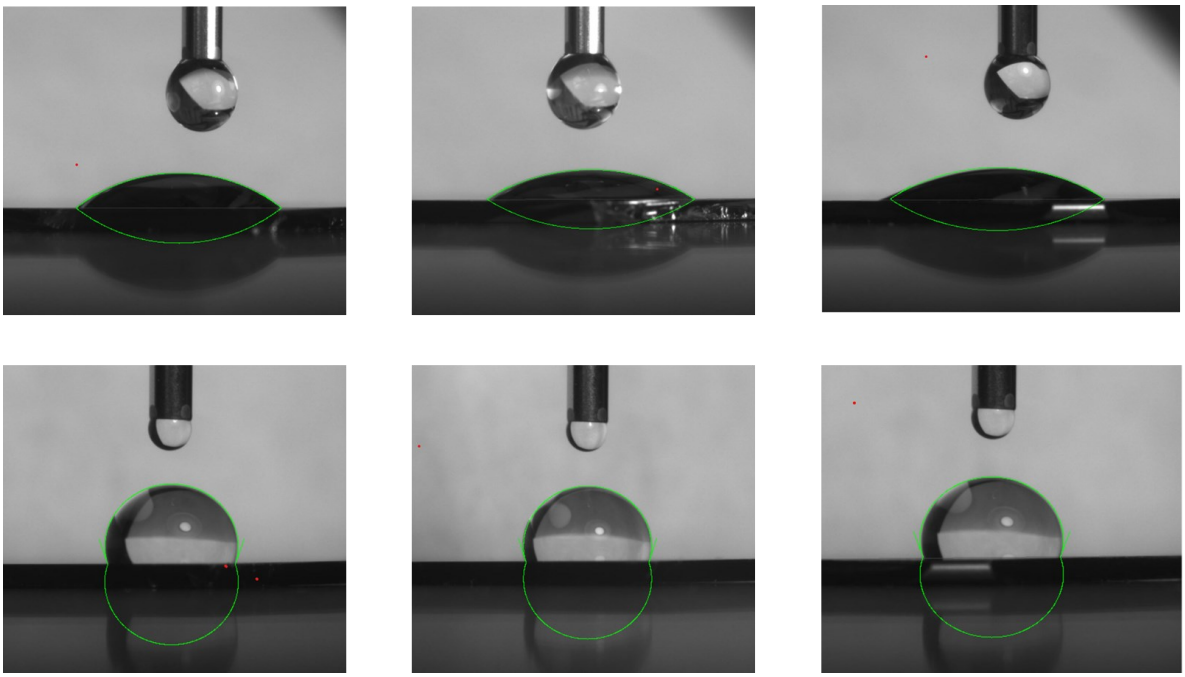

Figure 31: analysis of three water contact angles on the master after piranha souliìution cleaning (above) and silanization (below) to verify hydrophobicity was achieved

In the following table, the measured angles are reported.

	Meas. 1 (°)	Meas. 2 (°)	Meas. 3 (°)	Average (°)	St.Dev. (°)
Hydrophilicity	37	32	33	34	3
Hydrophobicity	111	108	110	109	2

Table 1

After cleaning with piranha solution, the contact angle was found to be 34 ± 3 °; the hydrophobic behavior is due to the pendent OH groups. The hydrophobicity was successfully obtained thanks to the self-assembled monolayer, as the contact angle was 109 ± 2 °.

The weight of the master was measured before and after the droplet deposition. The average volume of a droplet was 17±1 µl; as mentioned before, a droplet smaller than 16 µl could not be measured with this setup; thus, it could not be used for surface accurate tests. However, a smaller needle could be probably work for smaller droplets measures, and the dispensed droplet size distribution could also decrease.

4.2.UV curing of PEGDA and PPGDA: CNI-NILT tool calibration

Before the CNI tool was available, PEGDA and PPGDA had been cross-linked with a different tool, the Analytik Jena UV crosslinker. The tool has a chamber of dimensions 22.2 x 40.0 x 34.9 cm and 5 lamps with power 5 x 8 W on the inside of the lid; a sample can be placed at about 10 cm from the nearest lamp. A 1:99 photoinitiator to PEGDA or PPGDA ratio was found to be effective with a 60 minutes exposure for PEGDA and 90 minutes for PPGDA. A faster curing process was expected with the CNI NILT tool even though the power of its lamp was 12 W, as light absorption and reflection inside this chamber are lower in comparison to the other tool. Here, optimization of photo-activated curing of PEGDA and PPGDA is presented.

A peak at 1630-1640 cm^{-1} associated with CC double bond was expected to disappear after cross-linking completion; a 1:99 photoinitiated to PEGDA or PPGDA ratio was also used for these tests. The software Specragryph was used FTIR analysis.

The spectra of PEGDA and PEGDA solutions before curing are reported below (Graph 2).

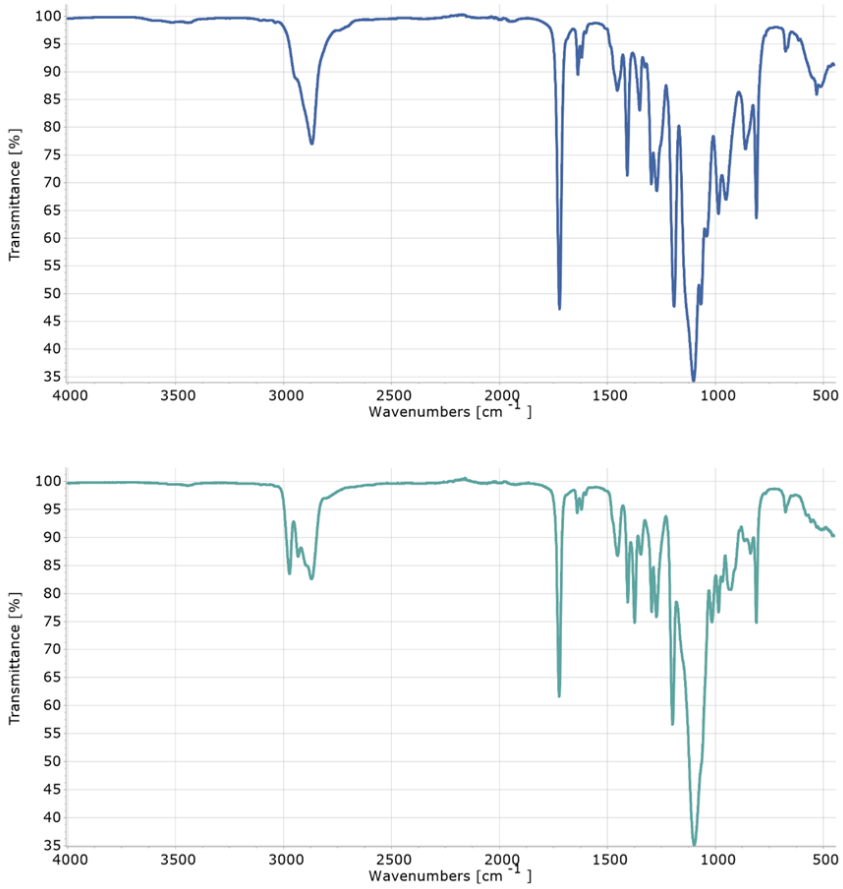

Graph 2: FTIR spectra of PEGDA (above) and PPGDA (below) before curing.

The spectra show strong peaks at 1721 cm^{-1} for both polymers, associated with the C=O bond in the acrylic group. A single peak can be seen in the PEGDA spectrum at 2869 cm^{-1} which was associated with the C-H stretching, while the PPGDA spectrum had 2 main peaks in the 2900-3000 cm^{-1} range: the same peak as for PEGDA at 2869 cm^{-1} and one at 2972 cm^{-1} were distinguishable; the latter is associated with the symmetric stretch of the methyl group side chain. The C=C bond peaks to be monitored were at 1636 cm^{-1} for PEGDA and 1639 cm^{-1} for PPGDA (stretching)[72,73]. Firstly, IR spectra of 15, 30, 45 minutes (PEGDA) and 15, 30, 45, and 60 minutes (PPGDA) UV lamp exposure samples were taken; the CC double bond peak disappeared in all the samples. For both PEGDA and PPGDA a peak at 1620cm^{-1} disappeared, therefore they

were associated to a band splitting due to cis-trans isomers; this interpretation was supported by a similar case in literature for C=C peak splitting in methyl acrylate[74]. Shorter exposures samples were examined: in order to define the best parameters to be used, a series of experiments were carried out with different timing and power percentages of the lamp: from 18 seconds exposure using the lamp at 10% of its power to 30 minutes using the full power; curing a sample for less than 18 seconds did not result in a solid product. For all the sets of experiments in which a 1-minute curing was taken as a control sample, it was enough to fully bring the cross-linking to completion for both PEGDA and PPGDA. Then, the lower limit was investigated with more accurate experiments, as follows.

4.2.1.*PEGDA*

In the following spectra (Graph 3), the CC double bond peak lowering in intensity indicates the disappearance of the acrylate groups, meaning that propagation took place. If the number of radicals forming under UV radiation is not sufficient to consume all the CC double bonds, the peak does not fully disappear after curing.

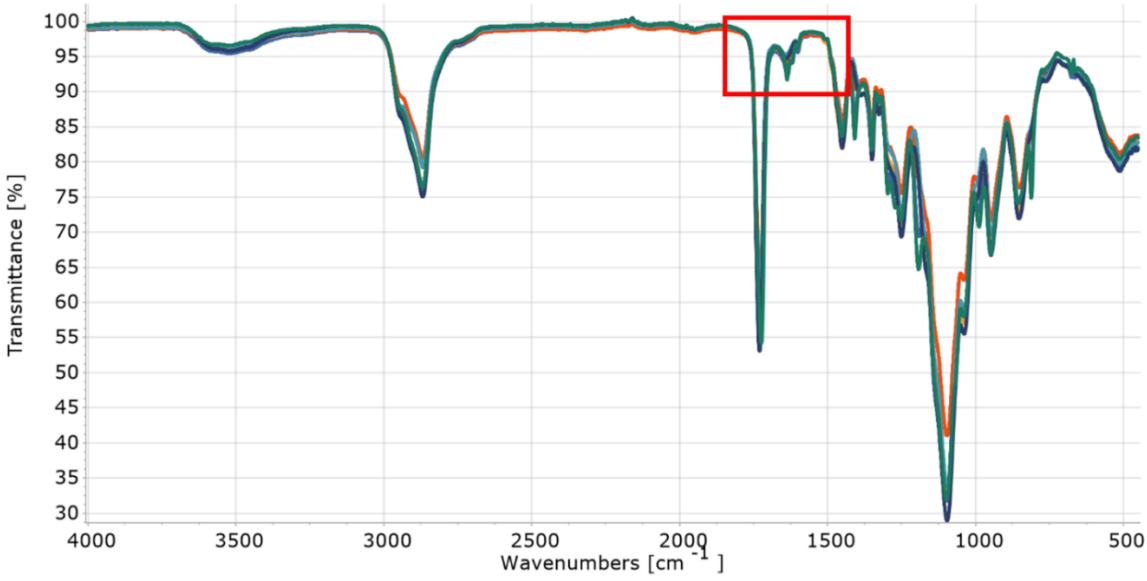

Graph 3: FTIR spectra of PEGDA for some cured samples; the region of the spectra to be monitored is highlighted by the red rectangle

The overlapped spectra correspond to different samples, that is different light power exposure and time of exposure as reported in Table 2:

Sample	Power percentage	time of exposure	Presence of peak
1	10%	18s	yes
2	10%	30s	yes
3	10%	60s	yes
4	40%	60s	no
5	70%	60s	No
6	100%	60s	No

Table 2

Zooming at the 1636 cm^{-1} peak (Graph 4: CC double bond peak):

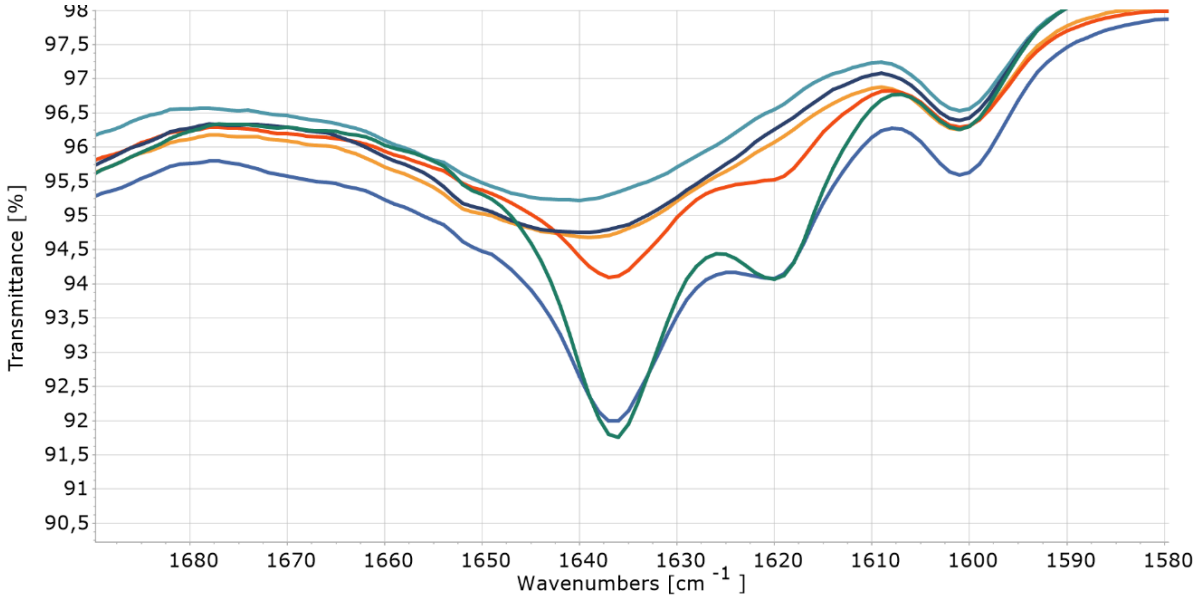

Graph 4: zoom at the 1636 cm^{-1} peak; sample 1 (dark green), sample 2 (dark blue), and sample 3 (red) still show presence of acrylate group; sample 4 (blue green), sample 5 (dark blue), and sample 6 (orange) cross-linking was led to completion.

Samples 1), 2), and 3) showed the presence of CC double bonds in the polymer, so the cross-link was prematurely interrupted. The peak disappeared in samples 4), 5), and 6) (the CC double bond was consumed). Therefore, a 1-minute exposure to UV radiation, 40% power, was enough to cross-link a 2,5 mm thick PEGDA sample (Graph 4). A weaker light or shorter exposure would

cause cross-links to form, but the network would not be complete. For consistency, 3 samples using the same parameters and 3 using 70% of the power were analyzed; none of them showed consistency, so 3 more sample using 100% of the power were analyzed, showing consistency. A significantly faster procedure for curing PEGDA than the previously used one was found.

4.2.2.*PPGDA*

The peak associated with the C=C bond in the acrylate group is found at 1639 cm^{-1} in PPGDA. A similar set of experiments to PEGDA ones were run. In the following, all the spectra (Graph 5):

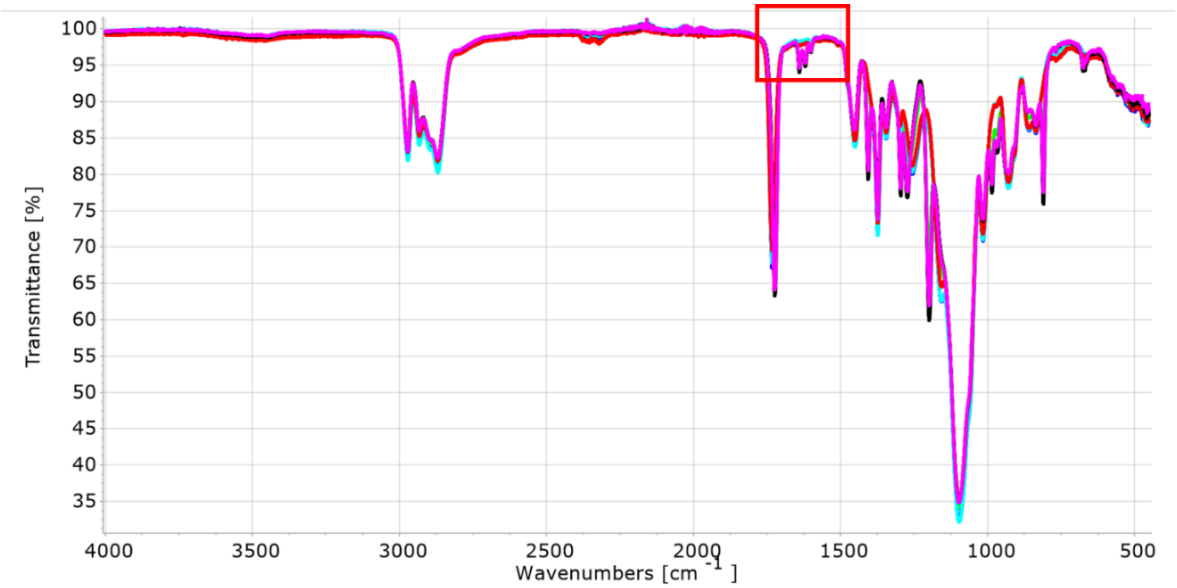

Graph 5: FTIR spectra of PPGDA for some cured samples; the region of the spectra to be monitored is highlighted by the red rectangle

The spectra correspond to different experiments, like in the previous case. Zooming at the 1639 cm^{-1} peak (Graph 6):

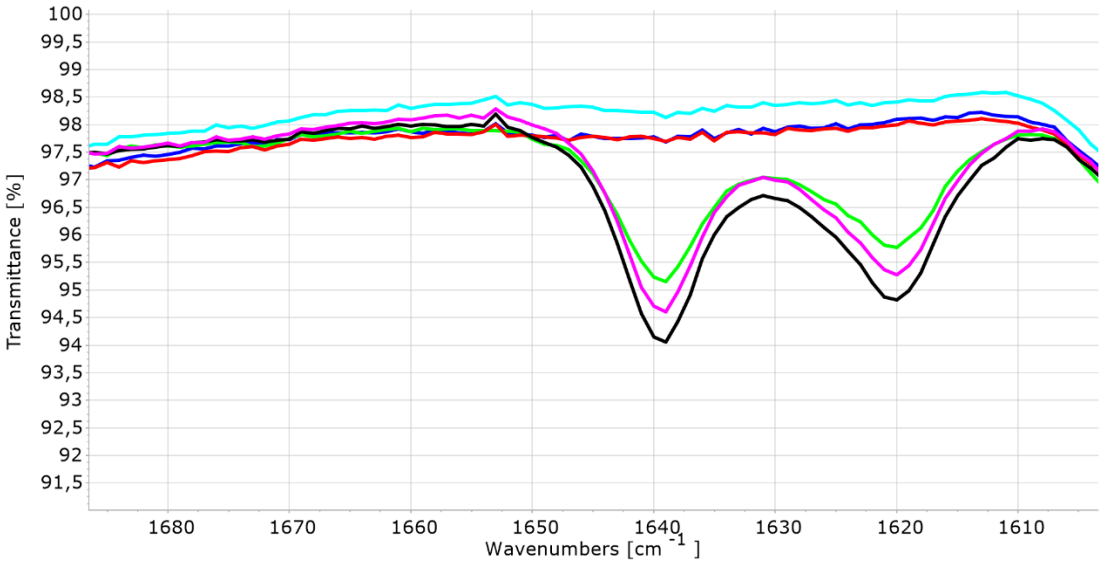

Graph 6: : zoom at the 1639 cm^{-1} peak; sample 1 (black), sample 2 (purple), and sample 3 (light green) still show presence of acrylate group; sample 4 (light blue), sample 5 (red), and sample 6 (blue) cross-linking was led to completion.

Sample	Power percentage	time of exposure	Presence of peak
1	10%	18s	yes
2	10%	30s	yes
3	10%	60s	yes
4	40%	60s	No
5	70%	60s	No
6	100%	60s	No

Table 3

As for PEGDA, samples 1), 2), and 3) showed the presence of the peak associated with the CC double bond in the acrylate group, while samples 4), 5) and 6) did not (Graph 6). Sample 1) cracked while applying pressure on it, so it was necessary to decrease the applied pressure to analyze it, but lowering the applied pressure could affect the measurement. Despite this, the peak was still visible.

To verify a change in the applied pressure between the sample and the diamond would not affect the measure significantly, 5 spectra of samples analyzed using different pressure were compared: the transmittance of peaks of interest did not change more than 3%.

As for the first PEGDA set of experiments, a 1-minute curing with 40% power was enough to fully consume the acrylate groups for a 2,5 mm thick PPGDA sample. For consistency, the same experiments as for PEGDA were conducted, but none of them had constant results. Even curing for 2 minutes using 100% of the power did not show constant results. For this reason, different areas of these samples were analyzed, and it was found that the cross-linking was not uniform; the unsuccessfulness of cross-linking could be then attributed to an uneven distribution of the photoinitiator in the solution because of its viscosity, so a new solution should be prepared and vigorously mixed before running the same experiments. Even though the validity of this procedure could not be verified, the results of the PEGDA analysis suggest that it would probably be confirmed by further experiments.

4.2.3.*Patterned primary molds*

The master with the cicada wing-inspired nanopattern was used as a stamp to obtain both PEG and PPG samples. AFM image of the master, patterned PEG and PPG (Fig.32), and SEM images of patterned PEG and PPG (Fig.33) are shown below.

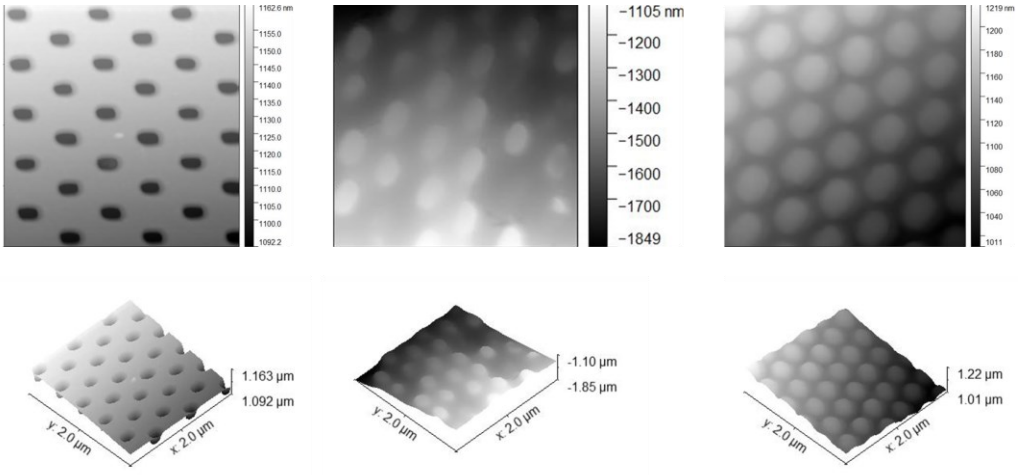

Figure 32: AFM images of the silicon master (left), patterned PEG (middle), and PPG (right)

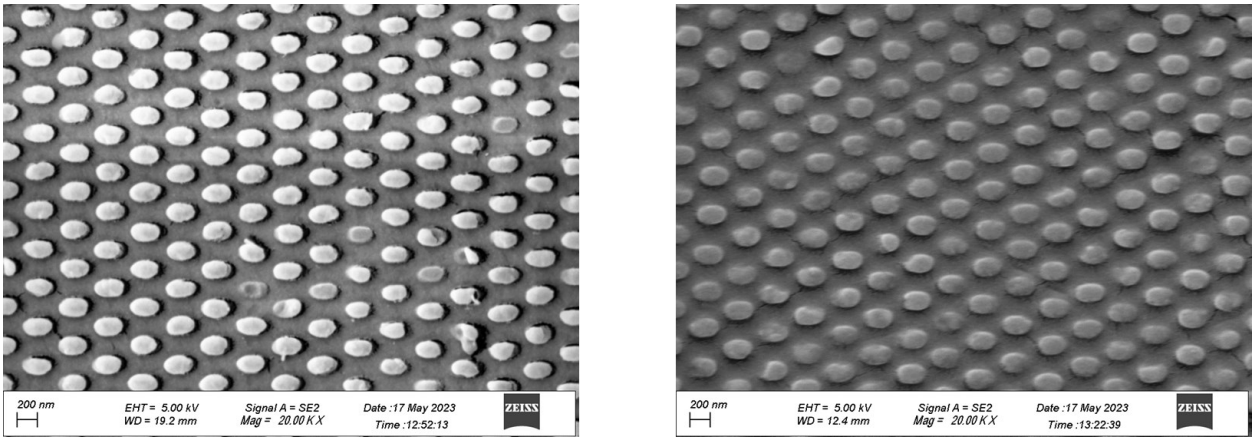

Figure 33: SEM images of patterned PEG (left) and PPG (right)

Cross-linked PEG and PPG were patterned in some regions of the sample; some other regions were not patterned at all or showed a coarse replica of the pattern. The reason for the patterning not being uniform across the sample could be the non-homogeneity of the self-assembled hydrophobic monolayer, or the breakage of the pillars' necks during the hand-demolding step.

More PEG and PPG replicas of the pattern should be made and analyzed; the master should be cleaned and silanized again before each experiment, to increase the chances to get a uniform monolayer of PFOCTS. In case the replica was still not uniform, AFM analysis of the master after the curing process could reveal the presence of cross-linked PEG or PPG fragments in the nanostructure cavities.

To analyze the quality of the motif of the nanopattern, the major axis of the ellipsoids were measured on 3 images for both PEG and PPG samples, 30 measures were taken for each image. The free software ImageJ was used for the analysis (Fig.34).

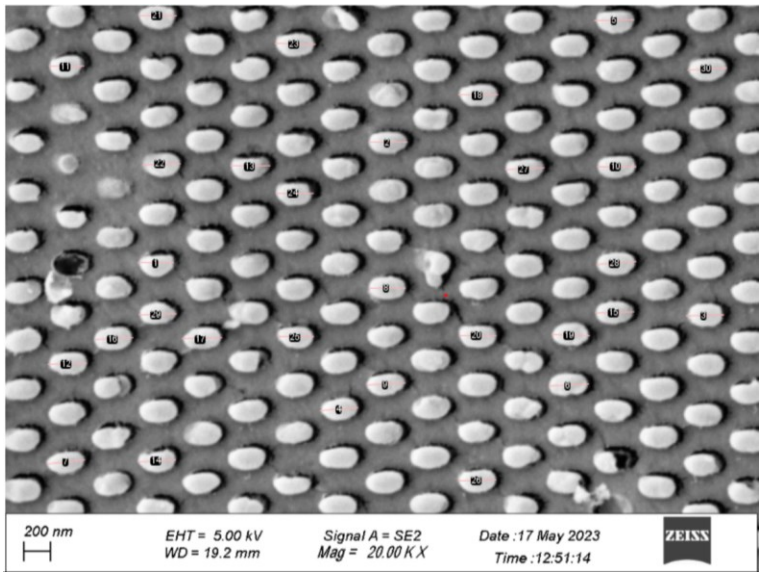

Figure 34: example of major axis analysis usin Imagej: single measures of the axis on a SEM image of patterned PEG

The average major measurement was 264 ± 13 nm for PEG and 266 ± 11 nm for PPG.

For both PEG and PPG the values were slightly bigger than the major axis of the ellipsoids of the master (250 nm); not all the surface was uniformly covered by the pattern, so more samples need to be analyzed and the un-patterned area, if still present, should be quantified. Despite the incomplete surface coverage, the overall molding was successful.

The height of the pillars and the depth of the holes on the master were estimated by analyzing the AFM images using the free software Gwyddion. In previous studies, it was found that the depth of the holes was 275 nm. The results were incoherent: the pillars in the PEGDA replica were found to be 120 ± 40 nm high, more than master's holes depth (49 ± 32 nm); the height of PPGDA replica pillars was 48 ± 18 nm. More so, the average height in every picture among the PEG sample, the PPG sample and the master were different to each other's, that is why the standard deviation was so high. In order to get a narrower distribution of heights and better measures, new samples should be prepared and analyzed. The AFM working parameters should probably be optimized before running other experiments. Also, PPG images seemed to have artifacts; the tip could be dragging some impurity while scanning, so this could explain the difference in height if compared to the master and the PEG sample.

4.3.Effect of pressure on mats

Applying pressure and temperature to membranes in a HE process could flatten the fibers, resulting in porosity loss and therefore membranes' efficiency reduction. The surface morphology reveals whether fibers undergo deformation under certain treatments; ensuring thermodynamic conditions are not sealing the pores or reducing their size, and studying the effect of T and p on the fibers is a needed step before HE experiments.

A big size dispersion of the fibers is intrinsically present in any PSF electrospun mat: in previous studies conducted by members of this group, it has been shown that the average diameter of the fibers tend to be bigger towards the center of the mat; in addition, the fibers themselves are very dispersed in size. In order to minimize differences in size in the samples to be analyzed, the pieces of the mat for any set of experiments were taken from a pre-selected region of the mats.

The effect of pressure alone was investigated first. 3 samples were tested, built as follows: the silicon master, a mat and a silicon slab on top were layered; a pressure of 0, 3, and 6 bar was applied respectively for 30 minutes; all the experiments were carried out under vacuum, and an as-spun piece of the mat was used as a control (Fig 35).

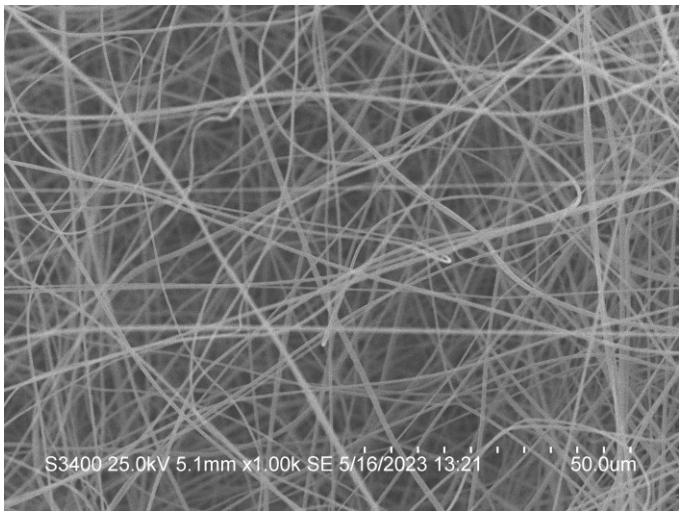

Figure 35: a SEM image of the as spun mat

Only the sample to which a 6 bar pressure was applied seemed to be different from the as-spun control mat surface (Fig. 36): more fibers than in other samples across the surface were closer to the same plane of the focal point of the SEM lens and could be detected. Measuring the thickness and tomography could prove the microstructure changed.

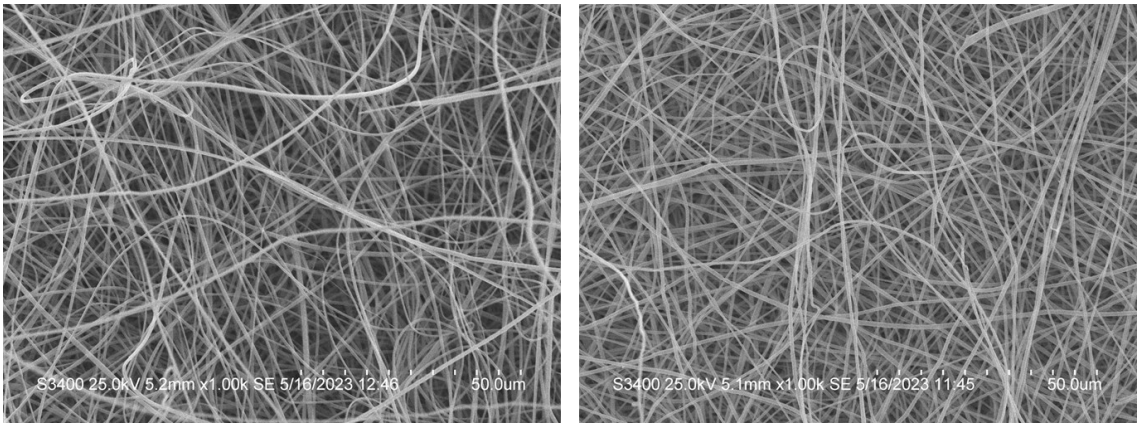

Figure36: SEM images of electrospun PSF surface after 30 minutes of treatment under 3 bar (left) and 6 bar (right).

The change in the average diameters of the fibers of different samples was studied, using the software ImageJ. Three SEM images of each sample were used for measurements.

The average fiber diameter was calculated and reported with standard deviation; 30 measurements were taken for each image, so 90 measurements for each sample (Fig.37);

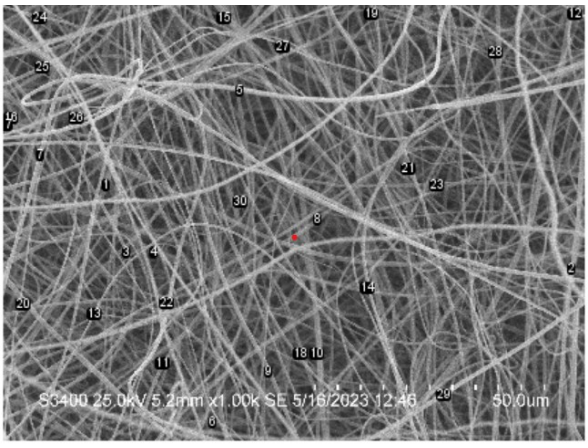

Figure 37: analysis of a SEM image using ImageJ: 30 fibers are chosen randomly

the average diameters of the fibers and standard deviations for each sample are reported in Table 5.

	Diameter (nm)	St.D. (nm)
As-spun	790	220
Only Vacuum	850	270
3 bar	820	260
6 bar	720	180

Table 4

Even though the mats pieces were taken from selected regions of the mat, the fibers showed a big variability in size, indeed standard deviations were over 25%. A big size dispersion and no visible change were expected; in order to verify this, more sets of experiments using the same applied pressure values must be carried out, and the resulting average fiber diameters should be compared to the control "as-spun fibers" with t-tests.

4.4.Effect of temperature and pressure on mats

Here, the same control sample used for tests described in the previous paragraph was used. The analysis was done the same way as described in the previous paragraph; 6 samples that were treated with p= 3 and p=6 bar were prepared, at T=140°C, 155°C and 170°C .

	pressure (bar)	Diameter (nm)	St.D. (nm)
As-spun	-	790	220
Only vacuum	-	850	270
T=140°C	3	1000	360
	6	971	350
T=155°C	3	720	230
	6	910	350
T=170°C	3	1280	610
	6	1040	310

Table 5

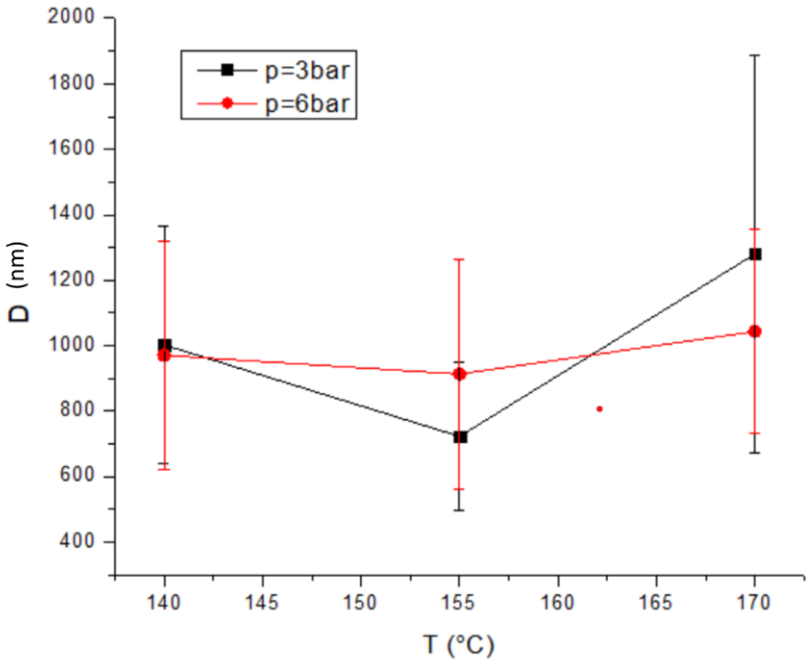

Graph 7: the effect of p and T on mats

The samples to which a pressure of 6 bar was applied did not show a big variation in their average fibers diameter; the diameters of the fibers in samples to which a pressure of 3 bar was applied changed dramatically (table 6 and Graph 7). Aside from the sample treated with 3 bar and 155°C, in all the others the average diameter had an increase on its standard deviation; in fact, some of the fibers that were closer to the surface in these samples were flattened, so the overall size dispersion raised.

The intrinsic size dispersion of the fibers makes it difficult to spot clear differences between the samples; in addition, uncontrollable variables related to the embossing procedure could explain this big variability of results, for instance some deformation during the stacking step. Another explanation could be the uneven distribution of stresses and temperature gradients when the pressure was applied, due to an imperfectly flat surface or to an asymmetrical stacking of the components.

These results cannot provide information to find any correlation between the applied temperature and pressure, and the diameter of the fibers after the treatment: more samples

using the same sets of parameters must be run, and the average fiber diameters must be compared to the control “as spun fibers” with t-tests.

4.5.Micropatterning of PSF electrospun Membranes

By using the same parameters as for the samples in the previous analysis, the micropattern was imprinted on mat cuts.

The wanted micropattern was a simple sequence of parallel 250 μm wide channels, and a 500 μm pitch (Fig.38).

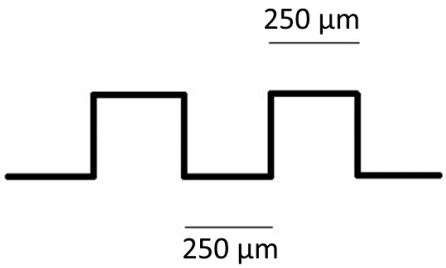

Figure 38: schematic representation of the wanted micropattern on the PLA to be 3D printed

Some images of the PDMS mold were taken to verify that the demolding step was successful; however, the micropattern geometry replica was not as expected (Fig.39).

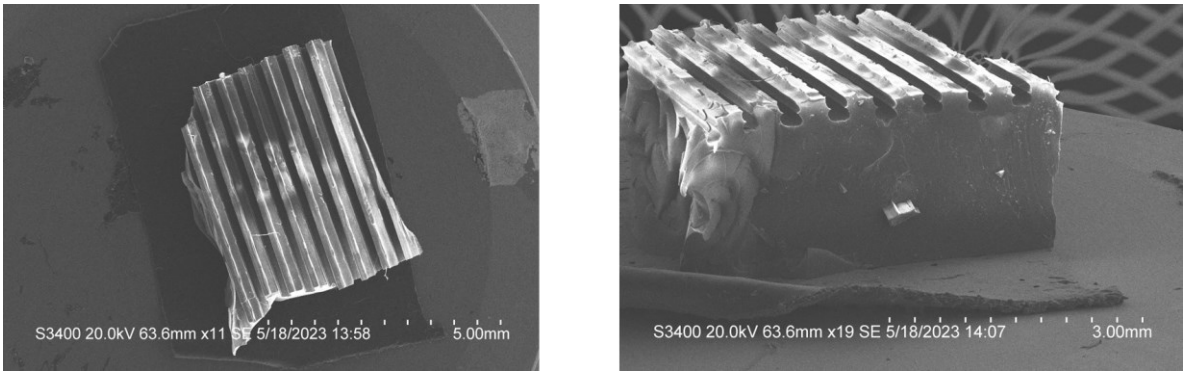

Figure 39: SEM images of the micropatterned PDMS

Despite the assumption of a good quality micropatterned PLA stamp, the reason for this was probably the PLA stamp itself, so SEM images of a new 3D printed PLA micropatterned piece for analysis were taken (Fig.40).

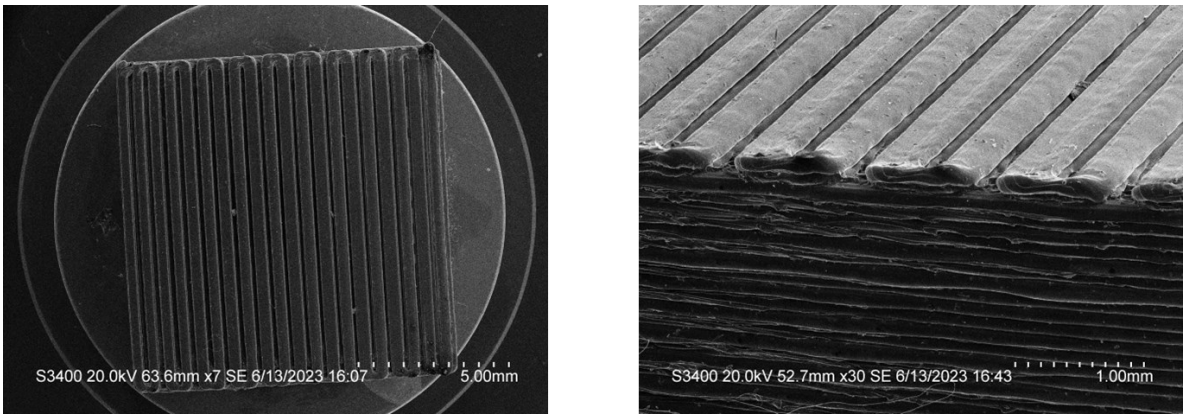

Figure 40: SEM images of the PLA sample that was printed for SEM analysis

The deviation from the desired pattern could be explained with the geometry of the PLA stamp. A perfect replica of the micropattern on the mats was not expected anyway, since the mats itself were even thinner than the micropattern channels. The imprinting of the nanopattern was attempted anyway, to see how the membranes would respond to this treatment.

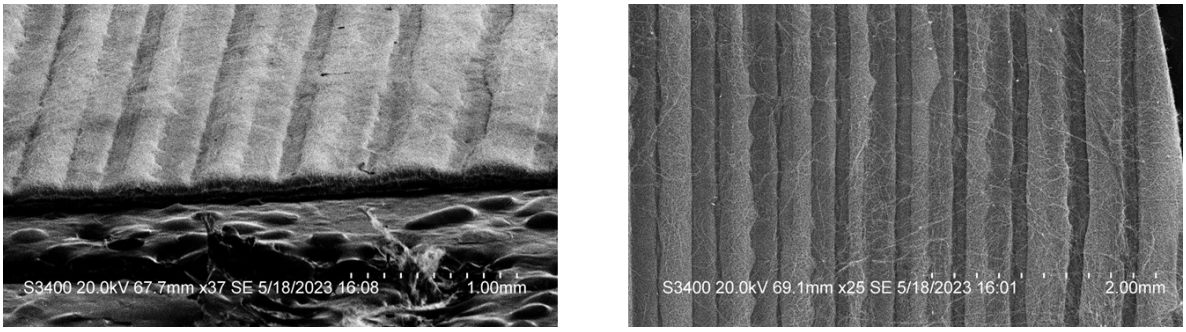

Figure 41: SEM images of a micropatterned piece of mat, attempt at T=155°C and p=3 bar; on the left, an image taken with a 75° tilt angle; on the right, a top view of the same sample.

A permanent microstructure was visible in every sample, but none of them showed an exact replica of the micropattern on them; the fibers probably could not reach the bottom of the

channels because of the thickness of the mats, and the pattern was not neat. The sample treated with T=155°C and p=3 bar is shown as an example (Fig.41). Applying pressure is probably not enough to push them into the channel as the thickness of a single mat itself is probably lower than the height of a channel in this micropattern. However, a permanent deformation was achieved in each sample, and the pitch of the employed pattern was at least 10 times bigger than the typical pitch of an anti-biofouling pattern; a micropattern with a lower pitch could be probably engraved on mats successfully.

4.6.Nanopatterning of PSF electrospun Membranes

Attempts at patterning mats with the Cicada wing-like nanopattern were made, using the silicon nanopatterned master available. A similar experimental procedure to the micropatterning was followed, as previously outlined in the Materials and Methods section.

A series of membranes were embossed at different T and p, aiming at identifying any set of parameters that was not far from giving a proper replica. To design this set of experiments, some possible pathways had to be taken into consideration: as for the micropatterning experiments, the temperature was assumed to be the most impactful factor. In order to minimize the polymer flow, so to minimize unwanted effects on fibers (flattening and broadening), a short embossing time and low pressures should be preferred; on the other hand, a longer embossing time and higher pressures could result in a better pattern. However, assuming there is an ideal embossing temperature for the PSF to soften enough to allow the pattern to form correctly, the overall effect was expected to be the flattening of fibers in any case.

Thus, just 1 minute was chosen as embossing time for this set of experiments and only two pressure values, 1 and 3 bar, lower than in micropatterning experiments. As follows (table 7, Graph 8), the average diameters of the fibers.

	pressure (bar)	Diameter (nm)	St.D. (nm)
As-spun	-	790	220
Only vacuum	-	850	270
T=135°C	1	1330	320
	3	730	210
T=145°C	1	1320	270
	3	550	150
T=155°C	1	1380	270
	3	880	220
T=165°C	1	700	190
	3	740	210
T=175°C	1	780	220
	3	760	280
T=185°C	1	1360	690
	3	840	300

Table 6

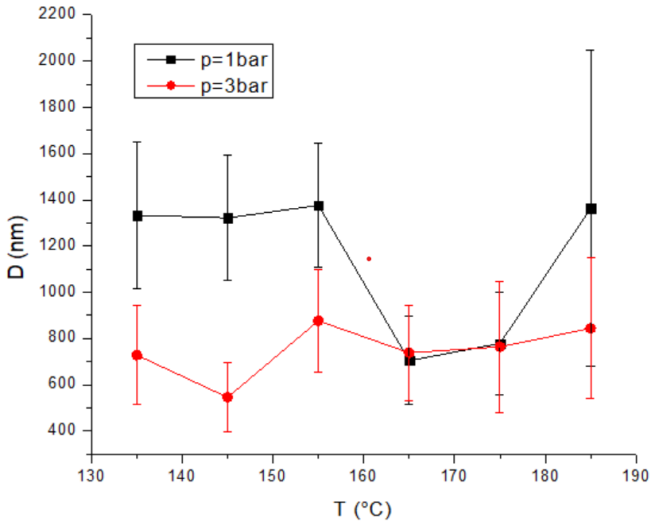

Graph 8: the effect on p and T on the nanopatterned mats

The samples to which a p=3 bar had been applied did not show major changes, whereas in the other set of experiments (p=1 bar) the samples treated with T=135°C, T=145°C, and T=155°C, the diameters were bigger compared to the other samples. Also the 185°C sample average fiber diameter was bigger than the reference and other samples; the reason was the flattening of

some of the fibers in this case; more so, the standard deviation was very high (Fig. 42). A Grubbs test was done to check if they could be considered as outliers, but the test rejected the hypothesis.

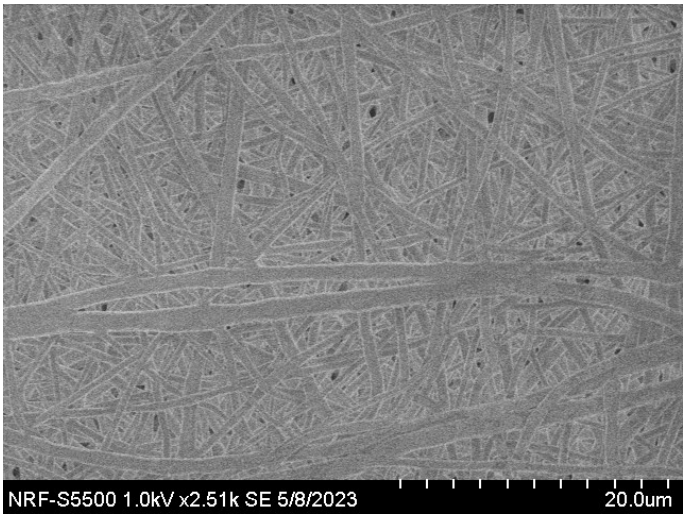

Figure 42: SEM image of the sample that was hot embossed for 1 minute, with p=3 bar and T=185°C

The fibers on the surface were clearly deformed, in some points new "necks" formed. The deeper fibers did not show the same behavior, as in general they were smaller than the surface fibers; however, they seemed to be sealed to each other in several points.

The nanopattern was visible in some region of the samples with the following parameters: T=165°C, p=3 bar; T=175°C, 1bar; T=175°C, 3 bar; T=185°C, 1 bar; T=185°C, 3 bar. Only in the last sample the pattern was on almost all the surface. A new set of experiments was carried out to find an optimized protocol for further tests: 6 samples using the same applied pressure parameters 1 bar and 3 bar, and T=175°C, 180°C and 185°C were embossed (Fig.43).

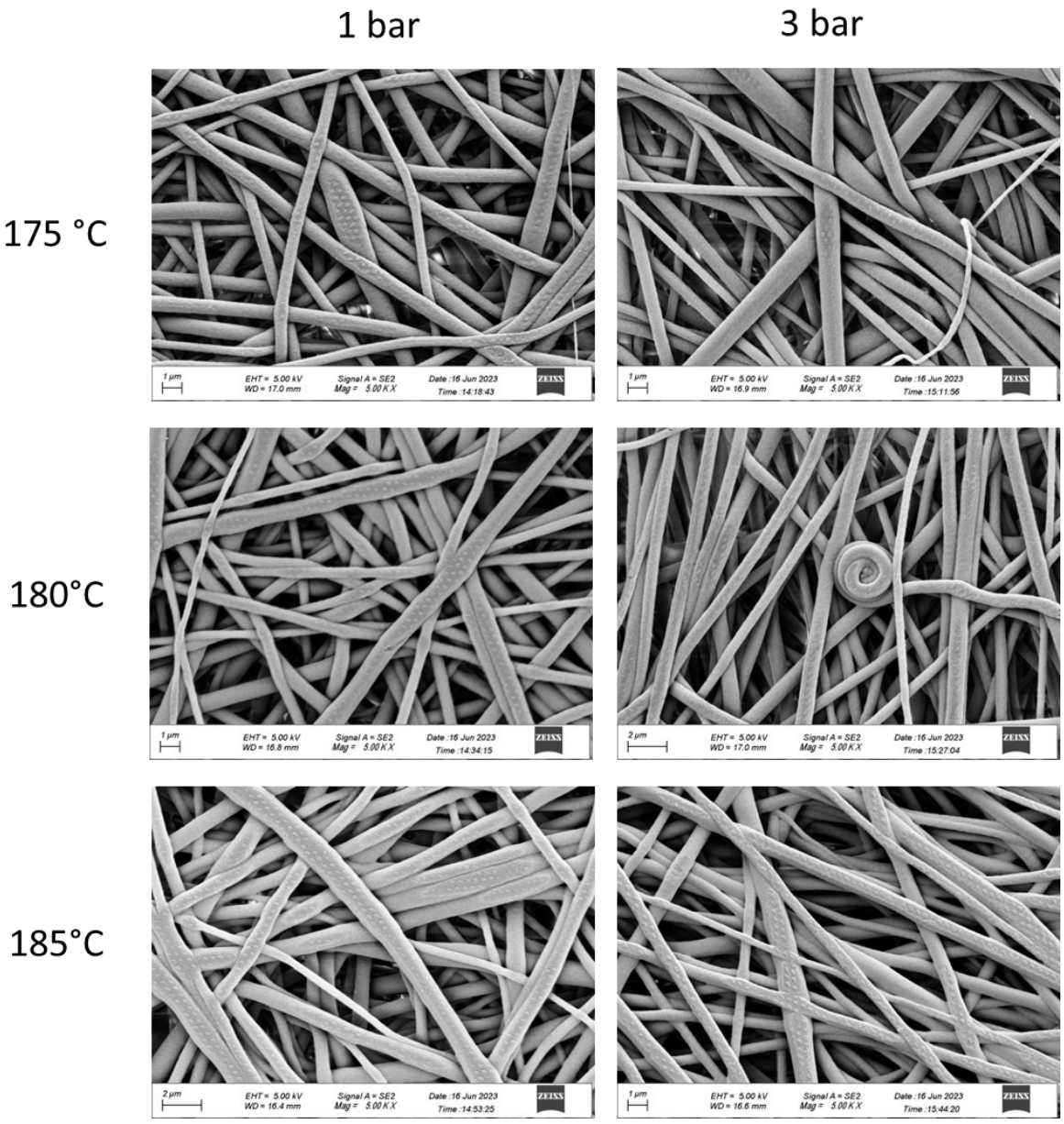

Figure 43: a set of HE experiments showing the imprinted nanopattern on some of the fibers

The pattern was in all the sample, and as in the previous set of experiments, the most covered surface (Fig.44) was obtained with p=3 bar and T=185°C.

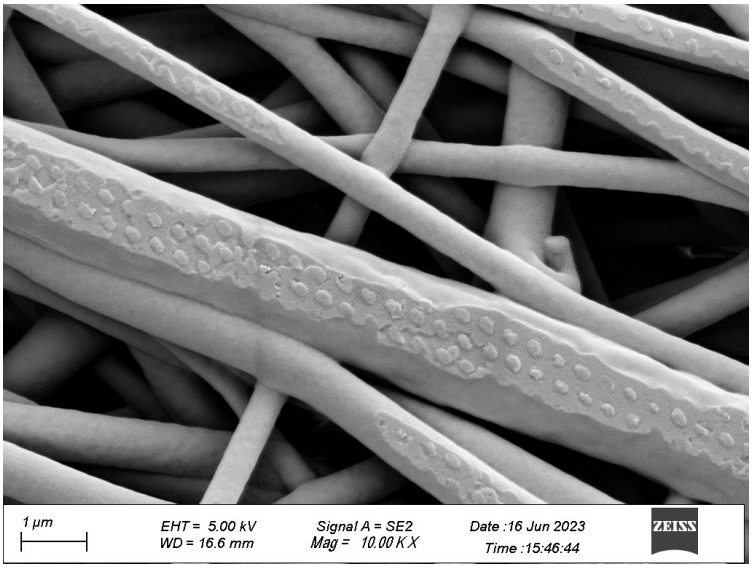

Figure 44: imprinted pattern on a fiber on the sample for which p=3 bar and T=185°C were used

The efficacy of these parameters must be proved with further experiments, and a way for quantifying the covered area is needed; then t-tests should be done to verify consistency. Anti-biofouling tests could finally be performed on the nanopatterned mats. Overall, these sets of experiments proved that imprinting a nanopattern on electrospun PSF mats via Hot Embossing is possible without sealing the pores; therefore, this clears the way for further research.

5. Conclusions

The present work aims at developing a procedure for engraving bioinspired micro- and nanostructured patterns on membranes for microfiltration via Hot Embossing. Firstly, the development of a standard procedure for cross-linking two polymers via UV radiation, PEGDA and PPGDA, was started; a procedure for PEGDA was found, while the procedure for PPGDA needs to be verified. Cross-linked PEG and PPG were used for replica molding of an antibacterial bioinspired nanopattern to create samples for antibacterial tests; the UV curing procedure was used to cross-link the polymers after casting the polymeric solution on a nanopatterned master; the resulting nanopatterned on the replica was not uniform; however, further experiments could bring to a standard method for better replicas. Secondly, the effect of temperature and pressure on the average diameter of electrospun PSF fibers were investigated; the experiments did not show major changes; however, further experiments should be run for verification; afterwards, attempts of engraving a simple micropattern on electrospun PSF mats via hot embossing were carried out; the samples did not show a good micropattern imitation, but had permanent deformation; a micropattern with smaller pitch, as most of the bioinspired anti-biofouling patterns have, is likely to give better results. Lastly, Hot Embossing experiments to imprint an antibacterial nanopattern (the same used for PEG and PPG replica) on PSF electrospun mats were conducted; on many samples that were treated with a temperature above 175°C, the nanopattern was imprinted on several portions of their surface. Two samples that were hot embossed under vacuum for 1 minute, with applied pressure 3 bar and embossing temperature 185°C had a uniform coverage; further investigation could start from finding whether these parameters work consistently and studying the quality of the patterned obtained in this way.

6. References and links

1. Sharifi, S. *Monitoring of Polyethylene Glycol-diacrylate-based Hydrogel Formation by Real Time NMR Spectroscopy*. www.SID.ir (2014).
2. Zhang, R. *et al.* Antifouling membranes for sustainable water purification: Strategies and mechanisms. *Chemical Society Reviews* vol. 45 5888–5924 Preprint at https://doi.org/10.1039/c5cs00579e (2016).
3. Selatile, M. K., Ray, S. S., Ojijo, V. & Sadiku, R. Recent developments in polymeric electrospun nanofibrous membranes for seawater desalination. *RSC Advances* vol. 8 37915–37938 Preprint at https://doi.org/10.1039/C8RA07489E (2018).
4. Mamah, S. C. *et al.* Recent development in modification of polysulfone membrane for water treatment application. *Journal of Water Process Engineering* vol. 40 Preprint at https://doi.org/10.1016/j.jwpe.2020.101835 (2021).
5. Tan, X. M. & Rodrigue, D. A review on porous polymeric membrane preparation. Part I: Production techniques with polysulfone and poly (vinylidene fluoride). *Polymers* vol. 11 Preprint at https://doi.org/10.3390/polym11071160 (2019).
6. Pendergast, M. M. & Hoek, E. M. V. A review of water treatment membrane nanotechnologies. *Energy and Environmental Science* vol. 4 1946–1971 Preprint at https://doi.org/10.1039/c0ee00541j (2011).
7. Giwa, A. The Applications of Membrane Operations in the Textile Industry: A Review. *Br J Appl Sci Technol* **2**, 296–310 (2012).
8. Zhang, X. *et al.* Recent advances in nature-inspired antifouling membranes for water purification. *Chemical Engineering Journal* **432**, (2022).
9. Díez, B. & Rosal, R. A critical review of membrane modification techniques for fouling and biofouling control in pressure-driven membrane processes. *Nanotechnology for Environmental Engineering* vol. 5 Preprint at https://doi.org/10.1007/s41204-020-00077-x (2020).
10. Zhang, X. *et al.* Recent advances in nature-inspired antifouling membranes for water purification. *Chemical Engineering Journal* **432**, (2022).
11. Costa, F. C. R. *et al.* Biofouling in membrane distillation applications - a review. *Desalination* vol. 516 Preprint at https://doi.org/10.1016/j.desal.2021.115241 (2021).
12. Oopath, S. V. *et al.* Nature-Inspired Biomimetic Surfaces for Controlling Bacterial Attachment and Biofilm Development. *Advanced Materials Interfaces* vol. 10 Preprint at https://doi.org/10.1002/admi.202201425 (2023).
13. Zhang, P., Lin, L., Zang, D., Guo, X. & Liu, M. Designing Bioinspired Anti-Biofouling Surfaces based on a Superwettability Strategy. *Small* **13**, (2017).
14. Sullivan, T. & O'callaghan, I. Recent developments in biomimetic antifouling materials: A review. *Biomimetics* vol. 5 1–16 Preprint at https://doi.org/10.3390/biomimetics5040058 (2020).

15. Bixler, G. D., Theiss, A., Bhushan, B. & Lee, S. C. Anti-fouling properties of microstructured surfaces bio-inspired by rice leaves and butterfly wings. *Journal of Colloid and Interface Science* vol. 419 114–133 Preprint at https://doi.org/10.1016/j.jcis.2013.12.019 (2014).

16. Damodaran, V. B. & Murthy, S. N. Bio-inspired strategies for designing antifouling biomaterials. *Biomater Res* **20**, (2016).

17. Maan, A. M. C., Hofman, A. H., de Vos, W. M. & Kamperman, M. Recent Developments and Practical Feasibility of Polymer-Based Antifouling Coatings. *Advanced Functional Materials* vol. 30 Preprint at https://doi.org/10.1002/adfm.202000936 (2020).

18. Gaur, M. S., Singh, P. K., Suruchi & Chauhan, R. S. Structural and thermal properties of polysulfone-ZnO nanocomposites. *J Therm Anal Calorim* **111**, 743–751 (2013).

19. Vilakati, G. D., Hoek, E. M. V. & Mamba, B. B. Probing the mechanical and thermal properties of polysulfone membranes modified with synthetic and natural polymer additives. *Polym Test* **34**, 202–210 (2014).

20. Chukov, D. *et al.* Structure, mechanical and thermal properties of polyphenylene sulfide and polysulfone impregnated carbon fiber composites. *Polymers (Basel)* **11**, (2019).

21. Parodi, F. *Step Polymerization*. *Comprehensive Polymer Science and Supplements* (1989).

22. Serbanescu, O. S., Voicu, S. I. & Thakur, V. K. Polysulfone functionalized membranes: Properties and challenges. *Materials Today Chemistry* vol. 17 Preprint at https://doi.org/10.1016/j.mtchem.2020.100302 (2020).

23. Pendergast, M. M. & Hoek, E. M. V. A review of water treatment membrane nanotechnologies. *Energy and Environmental Science* vol. 4 1946–1971 Preprint at https://doi.org/10.1039/c0ee00541j (2011).

24. Kelleher, S. M. *et al.* Cicada Wing Surface Topography: An Investigation into the Bactericidal Properties of Nanostructural Features. *ACS Appl Mater Interfaces* **8**, 14966–14974 (2016).

25. He, L., Lin, D., Wang, Y., Xiao, Y. & Che, J. Electroactive SWNT/PEGDA hybrid hydrogel coating for bio-electrode interface. *Colloids Surf B Biointerfaces* **87**, 273–279 (2011).

26. Chen, C. Y., Even, M. A., Wang, J. & Chen, Z. Sum frequency generation vibrational spectroscopy studies on molecular conformation of liquid polymers poly(ethylene glycol) and poly(propylene glycol) at different interfaces. *Macromolecules* **35**, 9130–9135 (2002).

27. Chen, R. T. *et al.* Photoinitiated alkyne-azide click and radical cross-linking reactions for the patterning of PEG hydrogels. *Biomacromolecules* **13**, 889–895 (2012).

28. Barron, V. *et al.* Development of chemically cross-linked hydrophilic-hydrophobic hydrogels for drug delivery applications. *Eur Polym J* **75**, 25–35 (2016).

29. Akram, N. *et al.* Spectroscopic, quantum chemical and molecular docking studies of 2-Hydroxy-4′-(2-hydroxyethoxy)-2-methylpropiophenone: A potent anti-Alzheimer's drug. *Chemical Data Collections* **29**, (2020).

30. Mazzarotta, A. *et al.* Small oligonucleotides detection in three-dimensional polymer network of dna-peg hydrogels. *Gels* **7**, (2021).

31. Andrzejewska, E. *Photopolymerization kinetics of multifunctional monomers*. www.elsevier.com/locate/ppolysci.

32. Wang, S., Liang, W., Dong, Z., Lee, V. G. B. & Li, W. J. Fabrication of Micrometer- and Nanometer-Scale polymer structures by visible light induced dielectrophoresis (DEP) force. *Micromachines (Basel)* **2**, 431–442 (2011).

33. Datta, S., Deshmukh, S. S., Kar, T. & Goswami, A. A review on modelling and numerical simulation of micro hot embossing process: fabrication, mold filling behavior, and demolding analysis. *Engineering Research Express* **5**, 012006 (2023).

34. Becker, H. & Heim, U. *Hot embossing as a method for the fabrication of polymer high aspect ratio structures*. *Sensors and Actuators* vol. 83 www.elsevier.nlrlocatersna (2000).

35. Deshmukh, S. S. & Goswami, A. Hot Embossing of polymers - A review. in *Materials Today: Proceedings* vol. 26 405–414 (Elsevier Ltd, 2019).

36. Oh, D. K. *et al.* Nanoimprint lithography for high-throughput fabrication of metasurfaces. *Frontiers of Optoelectronics* vol. 14 229–251 Preprint at https://doi.org/10.1007/s12200-021-1121-8 (2021).

37. Narasimhan, J. & Papautsky, I. Polymer embossing tools for rapid prototyping of plastic microfluidic devices. *Journal of Micromechanics and Microengineering* **14**, 96–103 (2004).

38. Sun, J. *et al.* Development and Application of Hot Embossing in Polymer Processing: A Review. *ES Materials and Manufacturing* vol. 6 3–17 Preprint at https://doi.org/10.30919/esmm5f605 (2019).

39. Kim, M., Moon, B. U. & Hidrovo, C. H. Enhancement of the thermo-mechanical properties of PDMS molds for the hot embossing of PMMA microfluidic devices. *Journal of Micromechanics and Microengineering* **23**, (2013).

40. Yun, D. & Kim, J. B. Material modeling of pmma film for hot embossing process. *Polymers (Basel)* **13**, (2021).

41. Çoğun, F., Yıldırım, E. & Sahir Arikan, M. A. Investigation on replication of microfluidic channels by hot embossing. *Materials and Manufacturing Processes* **32**, 1838–1844 (2017).

42. Li, J. M., Liu, C. & Peng, J. Effect of hot embossing process parameters on polymer flow and microchannel accuracy produced without vacuum. *J Mater Process Technol* **207**, 163–171 (2008).

43. Roos, N., Wissen, M., Glinsner, T. & Scheer, H.-C. *Impact of vacuum environment on the hot embossing process*. http://proceedings.spiedigitallibrary.org/ (2003).

44. Xue, J., Wu, T., Dai, Y. & Xia, Y. Electrospinning and electrospun nanofibers: Methods, materials, and applications. *Chemical Reviews* vol. 119 5298–5415 Preprint at https://doi.org/10.1021/acs.chemrev.8b00593 (2019).

45. Al-Abduljabbar, A. & Farooq, I. Electrospun Polymer Nanofibers: Processing, Properties, and Applications. *Polymers* vol. 15 Preprint at https://doi.org/10.3390/polym15010065 (2023).

46. Chen, H., Huang, M., Liu, Y., Meng, L. & Ma, M. Functionalized electrospun nanofiber membranes for water treatment: A review. *Science of the Total Environment* vol. 739 Preprint at https://doi.org/10.1016/j.scitotenv.2020.139944 (2020).

47. Kugarajah, V. *et al.* Future applications of electrospun nanofibers in pressure driven water treatment: A brief review and research update. *Journal of Environmental Chemical Engineering* vol. 9 Preprint at https://doi.org/10.1016/j.jece.2021.105107 (2021).

48. Drelich, J. W. Contact angles: From past mistakes to new developments through liquid-solid adhesion measurements. *Advances in Colloid and Interface Science* vol. 267 1–14 Preprint at https://doi.org/10.1016/j.cis.2019.02.002 (2019).

49. Wang, J., Wu, Y., Cao, Y., Li, G. & Liao, Y. Influence of surface roughness on contact angle hysteresis and spreading work. doi:10.1007/s00396-020-04680-x/Published.

50. Shastry, A., Abbasi, S., Epilepsia, A. & Böhringer, K. F. Contact angle hysteresis characterization of textured super-hydrophobic surfaces. in *TRANSDUCERS and EUROSENSORS '07 - 4th International Conference on Solid-State Sensors, Actuators and Microsystems* 599–602 (2007). doi:10.1109/SENSOR.2007.4300201.

51. Huhtamäki, T., Tian, X., Korhonen, J. T. & Ras, R. H. A. Surface-wetting characterization using contact-angle measurements. *Nat Protoc* **13**, 1521–1538 (2018).

52. Subhi, N., Verliefde, A. R. D., Chen, V. & Le-Clech, P. Assessment of physicochemical interactions in hollow fibre ultrafiltration membrane by contact angle analysis. *J Memb Sci* **403–404**, 32–40 (2012).

53. Wang, K., Abdala, A. A., Hilal, N. & Khraisheh, M. K. Mechanical Characterization of Membranes. in *Membrane Characterization* 259–306 (Elsevier Inc., 2017). doi:10.1016/B978-0-444-63776-5.00013-9.

54. Il Cha, D. *et al. Mechanical Behaviors and Characterization of Electrospun Polysulfone/Polyurethane Blend Nonwovens*. *Macromolecular Research* vol. 14 (2006).

55. Wang, K., Abdalla, A. A., Khaleel, M. A., Hilal, N. & Khraisheh, M. K. Mechanical properties of water desalination and wastewater treatment membranes. *Desalination* **401**, 190–205 (2017).

56. Da Silva Biron, D., Zeni, M., Bergmann, C. P. & Dos Santos, V. Analysis of composite membranes in the separation of emulsions sunflower oil/water. *Materials Research* **20**, 843–852 (2017).

57. Zhou, Z., Lin, W. & Wu, X. F. Electrospinning ultrathin continuous cellulose acetate fibers for high-flux water filtration. *Colloids Surf A Physicochem Eng Asp* **494**, 21–29 (2016).

58. Hakami, M. W. *et al.* Ceramic microfiltration membranes in wastewater treatment: Filtration behavior, fouling and prevention. *Membranes* vol. 10 1–34 Preprint at https://doi.org/10.3390/membranes10090248 (2020).

59. Tanis-Kanbur, M. B., Peinador, R. I., Calvo, J. I., Hernández, A. & Chew, J. W. Porosimetric membrane characterization techniques: A review. *Journal of Membrane Science* vol. 619 Preprint at https://doi.org/10.1016/j.memsci.2020.118750 (2021).

60. Peinador, R. I., Abba, O. & Calvo, J. I. Characterization of Commercial Gas Diffusion Layers (GDL) by Liquid Extrusion Porometry (LEP) and Gas Liquid Displacement Porometry (GLDP). *Membranes (Basel)* **12**, (2022).

61. Anovitz, L. M. & Cole, D. R. Characterization and analysis of porosity and pore structures. in *Pore Scale Geochemical Processes* 61–164 (De Gruyter, 2015). doi:10.2138/rmg.2015.80.04.

62. Tanis-Kanbur, M. B., Peinador, R. I., Hu, X., Calvo, J. I. & Chew, J. W. Membrane characterization via evapoporometry (EP) and liquid-liquid displacement porosimetry (LLDP) techniques. *J Memb Sci* **586**, 248–258 (2019).

63. Zhao, L. B., Xu, Z. L., Liu, M. & Wei, Y. M. Preparation and characterization of PSf hollow fiber membrane from PSf-HBPE-PEG400-NMP dope solution. *J Memb Sci* **454**, 184–192 (2014).

64. Berthomieu, C. & Hienerwadel, R. Fourier transform infrared (FTIR) spectroscopy. *Photosynthesis Research* vol. 101 157–170 Preprint at https://doi.org/10.1007/s11120-009-9439-x (2009).

65. Banerjee, A. Fourier Transform Infrared Spectroscopy-A Review. doi:10.13140/RG.2.2.16082.89282.

66. Ng, L. M. & Simmons, R. Infrared spectroscopy. *Anal Chem* **71**, (1999).

67. Mohammed, A. & Abdullah, A. *SCANNING ELECTRON MICROSCOPY (SEM): A REVIEW*.

68. Xu, N. S. & Huq, S. E. Novel cold cathode materials and applications. *Materials Science and Engineering R: Reports* vol. 48 47–189 Preprint at https://doi.org/10.1016/j.mser.2004.12.001 (2005).

69. Binnig, G., Quate' ', C. F., Gi, E. L. & Gerber, C. *Atomic Force Microscope*.

70. Jalili, N. & Laxminarayana, K. A review of atomic force microscopy imaging systems: Application to molecular metrology and biological sciences. *Mechatronics* **14**, 907–945 (2004).

71. Badv, M., Jaffer, I. H., Weitz, J. I. & Didar, T. F. An omniphobic lubricant-infused coating produced by chemical vapor deposition of hydrophobic organosilanes attenuates clotting on catheter surfaces. *Sci Rep* **7**, (2017).

72. Sharifi, S. *Monitoring of Polyethylene Glycol-diacrylate-based Hydrogel Formation by Real Time NMR Spectroscopy*. www.SID.ir (2014).

73. Chen, C. Y., Even, M. A., Wang, J. & Chen, Z. Sum frequency generation vibrational spectroscopy studies on molecular conformation of liquid polymers poly(ethylene glycol) and poly(propylene glycol) at different interfaces. *Macromolecules* **35**, 9130–9135 (2002).

74. Carmona, P. & Imoreno, J. *THE INFRARED SPECTRA AND STRUCTURE OF METHYL ACRYLATE*.

Links

1. https://www.auroraprosci.com/Introduction-FTIR-ATR-Fiber-Optics-ATR-Probes-in-Spectroscopy-Part-I